Materials Advances

COMMUNICATION

Check for updates

An eco-friendly K₂NaInBr₆ double halide perovskite as a next-generation absorber for perovskite solar cells: a DFT and SCAPS-1D study

Nazmul Shahadath,[a] Ashraful Mujahid, [iD][a] Raihan Kabir,[a] Md. Tarekuzzaman, [iD][a] Mohammad Yasin Hayat Khan,[a] Md. Abu Bakkar Siddique,[a] Sohail Ahmad,[b] Md. Rasheduzzaman[a] and Md. Zahid Hasan [iD] *[a]

Environmental drawbacks of lead-based perovskite solar cells (PSCs) have driven growing interest in eco-friendly double halide compounds, notably $K_2NaInBr_6$. This study presents a comprehensive investigation of the structural, electronic, and optical properties of $K_2NaInBr_6$ using density functional theory (DFT), with the obtained results further employed to evaluate its potential as an absorber layer in solar cell applications. Structural analysis confirms the cubic symmetry of $K_2NaInBr_6$, while its electronic band structure and density of states (DOS) indicate semiconductive behavior, with band gaps of 1.99 eV (PBE) and 1.89 eV (PBEsol). Evaluation of optical behavior from 0 to 12 eV, using PBEsol and PBE formalisms, indicates that the absorption coefficient, reflectivity, refractive index, dielectric function, optical conductivity, and energy loss collectively endorse the material as an excellent light absorber. The suitability of $K_2NaInBr_6$ for solar cell applications was tested by modeling a range of device architectures using SCAPS-1D. In the comparative study of 24 device structures, the $ITO/SnS_2/K_2NaInBr_6/Cu_2O/Ni$ design exhibited superior performance, yielding a power conversion efficiency (PCE) of 21.9%, an open-circuit voltage (V_{OC}) of 1.56 V, a short-circuit current density (J_{SC}) of 15.92 mA cm^{-2}, and a fill factor (FF) of 87.75%. Contour mapping was utilized to determine how absorber and ETL thicknesses affect fundamental photovoltaic responses. The investigation extends to analyzing the influence of eight LMCs (left metal contacts), series and shunt resistances, temperature variations, quantum efficiency (QE), capacitance–voltage (C–V) response, generation and recombination effects, Mott–Schottky characteristics, current density–voltage (J–V) behavior, and impedance characteristics on device performance. The extraordinary photon capture performance of the $K_2NaInBr_6$ perovskite highlights its importance for improving photovoltaic and optoelectronic devices.

1. Introduction

The global community faces an urgent need to transition toward clean and renewable energy sources due to the combined pressures of rising energy demand, depletion of fossil fuel reserves, and environmental degradation.[1,2] Fossil fuels such as coal, oil, and natural gas, while still meeting the majority of the world's energy needs, pose serious environmental threats, including greenhouse gas emissions and ecological damage.[3,4] In addition, geopolitical instability surrounding fossil fuel extraction further threatens global energy security.[5] These concerns have intensified research into sustainable and environmentally safe energy systems capable of providing long-term stability.[6–8] As a result, the focus of global research has increasingly shifted toward identifying sustainable, renewable, and environmentally responsible alternatives. Among the various renewable sources, solar energy stands out as a clean, abundant, and highly reliable option, prompting rapid advancements in photovoltaic (PV) technology.[9–11] PV technology, which directly converts sunlight into electricity, is therefore a pivotal contributor to the global shift toward sustainable energy solutions.[12]

The first application of a lead–halide perovskite material, $CH_3NH_3PbBr_3$, in a photovoltaic device was reported by Miyasaka *et al.*, achieving a power conversion efficiency (PCE) of 2.2%.[13] This performance was later enhanced to 3.8% by substituting iodine for bromine.[14] The breakthrough for solid-state PSCs occurred in 2012, when Kim and colleagues achieved a PCE of 9.7% using spiro-MeOTAD as the hole transport layer (HTL).[15] Within a few years, advancements in composition engineering and thin-film deposition techniques enabled certified PCEs exceeding 23%.[16,17]

[a] *Materials Research and Simulation Lab, Department of Electrical and Electronic Engineering, International Islamic University Chittagong, Kumira, Chittagong, 4318, Bangladesh. E-mail: zahidhasan.02@gmail.com*

[b] *Department of Physics, College of Science, King Khalid University, P O Box 9004, Abha, Saudi Arabia*

In the pursuit of stable and non-toxic alternatives to lead-based perovskites, double perovskites (DPs) with the general formula $A_2M'M''X_6$ (A is a monovalent cation, M' is a monovalent, M'' is a trivalent cation, and X is a halide anion)[18] have emerged as promising candidates due to their greater structural stability, tunable electronic properties,[19] and high theoretical PCE approaching 30%.[20] Notably, compounds such as $Cs_2AgBiBr_6$, $Cs_2CuSbCl_6$, and La_2NiMnO_6 have shown potential for achieving efficiencies above 20%, i.e., 23.5%,[21] 21.67%,[22] and 20.18%,[23] respectively, when optimized through simulation frameworks like SCAPS-1D. Sangavi et al. conducted comprehensive theoretical and experimental investigations on the double perovskite La_2NiMnO_6, achieving simulated and experimental PCEs of about 10% and 4.5%, respectively.[24] Double perovskites also address limitations in conventional PSCs by reducing hysteresis, enhancing thermal stability, and enabling environmentally safe device architectures.[25–29]

The rapid improvement of PSC performance can be attributed to careful optimization of device components, particularly the electron transport layers (ETLs) and HTLs, which play critical roles in charge extraction, stability, and interface compatibility. HTL materials such as spiro-MeOTAD, Cu_2O, CuSCN, $CuSbS_2$, NiO, P_3HT, V_2O_5, and PEDOT:PSS are widely investigated due to their tunability and efficient hole transport, but they often face issues such as high processing costs, poor stability, and low conductivity.[30,31] Similarly, ETL materials must offer excellent electron mobility, energy-level alignment, and cost-effectiveness,[32] and common ETLs include TiO_2, ZnO, SnO_2, WO_3, PCBM, and Al_2O_3.[33,34] Many studies have demonstrated that optimizing ETL–HTL combinations with appropriate absorber layers can significantly enhance PSC performance.[35–37]

Both theoretical and experimental works have been dedicated to understanding the photovoltaic potential of DPs.[38] Although theoretical simulations often predict enhanced photovoltaic performance, achieving comparable efficiencies experimentally remains challenging for perovskite solar cells. This discrepancy arises from practical limitations such as material defects, interfacial losses, and stability issues that are difficult to fully capture in idealized models. For example, Zhang et al. and Alanazi et al. reported theoretical PCEs of 6.37% and 14.29%, respectively, for $Cs_2AgBiBr_6$-based devices employing SnO_2 and spiro-MeOTAD as the ETL and HTL, respectively.[39]

A comprehensive understanding of the electronic properties of double perovskites, such as density of states (DOS), charge distribution, and band structure, is essential for tailoring their optoelectronic behavior.[40] DPs exhibit favorable optical absorption, long carrier lifetimes, and structural robustness, making them highly attractive for both solar energy and broader optoelectronic applications.[41,42] Computational approaches, particularly density functional theory (DFT), have become indispensable in this research domain. First-principles simulations allow accurate predictions of the band structure, DOS, optical spectra, and defect energetics.[43,44] Additionally, device-level simulation tools like SCAPS-1D facilitate performance modeling of complete solar cell architectures, enabling prediction of parameters such as open-circuit voltage (V_{OC}), short-circuit current density (J_{SC}), fill factor (FF), and overall PCE under various design conditions.[45,46] These theoretical methods reduce reliance on costly experimental trial-and-error, accelerating the development of high-efficiency, stable PSCs.[47,48]

Recent studies have explored the structural, electronic, and optical characteristics of novel lead-free DPs (double perovskites) for solar applications. For instance, $K_2NaInBr_6$ has attracted attention for its suitable band gap, chemical stability, and environmentally benign composition. In the present work, we employ first-principles DFT calculations to analyze its electronic and optical properties, complemented by SCAPS-1D simulations to evaluate device-level performance. Prior DFT studies of this compound utilized GGA and LDA; however, the present study employs PBE and PBE-sol to achieve enhanced accuracy.[49] Multiple ETLs (TiO_2, ZnO, LBSO, and SnS_2), HTLs (Cu_2O, CdTe, Cu_2Te, CBTS, CuI, and spiro-MeOTAD) and LMCs (Cu, Fe, C, Au, W, Ni, Pd, Pt, and Se) are examined in combination with Al as the right contact, with key parameters such as absorber thickness, recombination rates, quantum efficiency, and J–V characteristics assessed. The objective is to evaluate the suitability of $K_2NaInBr_6$ as a lead-free absorber for high-efficiency PSCs and broader optoelectronic applications.

2. Materials and methodology

2.1 First-principles calculations of the $K_2NaInBr_6$ absorber using DFT

In this study, the optoelectronic and structural properties of the $K_2NaInBr_6$ perovskite absorber were investigated using density functional theory (DFT) implemented in the WIEN2k simulation package. The calculations were performed within the full-potential linearized augmented plane wave (FP-LAPW) framework.[50] The computational workflow consisted of three main stages: (i) structural optimization, (ii) evaluation of electronic properties, and (iii) calculation of optoelectronic parameters.

For the structural relaxation, the generalized gradient approximation (GGA) was applied using the Perdew–Burke–Ernzerhof (PBE) exchange–correlation functional.[51] The total energy was converged by optimizing the basis set size with $R \times K_{max} = 8$, $G_{max} = 14$ and employing a $10 \times 10 \times 10$ k-point mesh. The convergence threshold for total energy was fixed at 10^{-6} Ry.

To accurately predict the bandgap, the PBEsol potential was utilized.[52] The semiclassical transport coefficients were determined using the relaxation time approximation (RTA) with a fixed relaxation time of 10^{-14} s. The mathematical expressions for the optical parameters, including refractive index, absorption coefficient, and reflectivity, were derived following standard formulations given in eqn (1)–(6).[53,54]

$$\varepsilon_1(\omega) = \frac{2}{\pi} P \int_0^\infty \frac{\omega' \varepsilon_2(\omega')}{\omega'^2 - \omega^2} d\omega' + 1 \qquad (1)$$

$$\varepsilon_2(\omega) = \frac{2\pi e^2}{\Omega\varepsilon_0}\sum_{k,v,c}\left|\langle\psi_k^c|\hat{u}\hat{r}|\psi_k^c\rangle\right|^2\delta\left(E_k^c - E_k^v - E\right) \quad (2)$$

$$\alpha(\omega) = \sqrt{2\omega\left[\sqrt{\varepsilon_1^2(\omega) + \varepsilon_1^2(\omega)} - \varepsilon_1(\omega)\right]^{1/2}} \quad (3)$$

$$n(\omega) = \left[\frac{\varepsilon_1(\omega) + \varepsilon_2^2(\omega)^{1/2}}{2} + \frac{\varepsilon_1(\omega)}{2}\right]^{1/2} \quad (4)$$

$$R(\omega) = \left[\frac{\varepsilon(\omega)^{\frac{1}{2}} - 1}{\varepsilon(\omega)^{\frac{1}{2}} - 1}\right]^2 \quad (5)$$

$$L(\omega) = \left[\frac{\varepsilon_2(\omega)}{\varepsilon_1^2(\omega) + \varepsilon_2^2(\omega)}\right] \quad (6)$$

The symbols represent the real component of the dielectric function $\varepsilon_1(\omega)$, the imaginary component $\varepsilon_2(\omega)$, the absorption coefficient $\alpha(\omega)$, the refractive index $n(\omega)$, the reflectivity $R(\omega)$, and the energy loss function $L(\omega)$.

2.2 SCAPS-1D numerical simulations

Numerical device modeling was conducted using the SCAPS-1D simulator to understand the working mechanisms of the designed solar cells and to identify the parameters influencing their performance. SCAPS-1D solves the one-dimensional semiconductor transport problem by integrating Poisson's equation (eqn (7))[55] with the continuity equations for electrons (eqn (8)) and holes (eqn (9)), ensuring charge conservation within the device.

$$\frac{\partial n}{\partial x}\varepsilon(x)\frac{\partial\psi}{\partial x} = \frac{-q}{\varepsilon_0}\left[p - n + N_D^+ - N_A^- + \frac{\rho_{\text{def}}(n,p)}{q}\right] \quad (7)$$

$$\frac{\partial n}{\partial t} = -\frac{\partial J_n}{\partial x} + G - U_n(n,p) \quad (8)$$

$$\frac{\partial p}{\partial t} = -\frac{\partial J_p}{\partial x} + G - U_p(n,p) \quad (9)$$

In these formulations, ψ denotes the electrostatic potential, ε is the dielectric constant, q is the elementary charge, and ρ_{def} represents the defect charge density. The terms p and n indicate the hole and electron concentrations, respectively, while N_D and N_A are the donor and acceptor doping densities. The current densities for electrons and holes were calculated using the drift–diffusion equations (eqn (10) and (11)),[56] where μ_n and μ_p represent mobilities and D_n and D_p are diffusion coefficients derived from the Einstein relation.

$$J_n = q\mu_n n\varepsilon + qD_n\partial n \quad (10)$$

$$J_p = q\mu_p p\varepsilon + qD_p\partial p \quad (11)$$

The absorption coefficient was evaluated using an improved E_g-sqrt model, which refines the conventional $\sqrt{h\nu - E_g}$ approach, as expressed in eqn (12).[55] This method follows the Tauc relation for direct and indirect bandgap materials.

Furthermore, the dependence of the absorption profile on bandgap energy was parameterized using α_0 and β_0, as shown in eqn (13) and (14).[57]

$$\alpha(h\nu) = \left(\alpha_0 + \beta_0\frac{E_g}{h\nu}\right)\sqrt{\frac{h\nu}{E_g} - 1} \quad (12)$$

$$\alpha_0 = A\sqrt{E_g} \quad (13)$$

$$\beta_0 = B\frac{1}{\sqrt{E_g}} \quad (14)$$

The SCAPS-1D simulation workflow is summarized in Fig. 1, comprising six sequential steps. The solar cell structure was modeled with $K_2NaInBr_6$ as the absorber layer, sandwiched between suitable electron transport layers (ETLs) and hole transport layers (HTLs). The simulation accounted for material properties such as bandgap, dielectric constant, electron affinity, and carrier mobilities, as well as external conditions like temperature, illumination spectrum (AM 1.5G), and voltage sweep ranges for J–V characterization. The main physical and electrical characteristics of solar cell materials, such as ITO, ETLs, $K_2NaInBr_6$, and HTLs, are summarized in Tables 1–3. These characteristics are bandgap, dielectric constant, electron affinity, and carrier mobility, which have an influence on V_{OC} and PCE and are essential for SCAPS-1D simulations. Interface defects at ETL/absorber and absorber/HTL boundaries were also considered, with defect densities and capture cross-sections defined in Table 3, as they play a key role in non-radiative recombination losses. By varying ETL/HTL types, layer thicknesses, and defect densities, the influence of each factor on open-circuit voltage (V_{OC}), short-circuit current density (J_{SC}), fill factor (FF), and power conversion efficiency (PCE) was assessed. The optimal configuration was identified based on the highest simulated PCE values.

2.3 Synergy between SCAPS simulation and DFT theory

The correlation between SCAPS (solar cell capacitance simulator) and density functional theory (DFT) plays a vital role in bridging material-level properties with device-level performance in the field of photovoltaic technology. DFT is a quantum mechanical method that provides detailed insights into the electronic structure of materials, including band gap (E_g (eV)), electron affinity (X (eV)), relative dielectric permittivity (ε_r), effective mass (N_c (cm^{-3}) and N_v (cm^{-3})), and carrier mobilities (μ, electron mobility (μ_n, cm^2 V^{-1} s^{-1}) and hole mobility (μ_h cm^2 V^{-1} s^{-1})), which are directly used as physically consistent inputs in SCAPS-1D. A similar combined DFT–SCAPS-1D approach has been adopted in previous studies, where the same methodology was followed to achieve optimized device performance.[63] This approach ensures a reliable link between the microscopic electronic structure and macroscopic device performance and is commonly adopted in perovskite solar cell modeling. SCAPS, on the other hand, is a numerical simulation tool designed to model the electrical behavior of complete solar cell structures, considering layers, interfaces, defects, and recombination mechanisms. By feeding
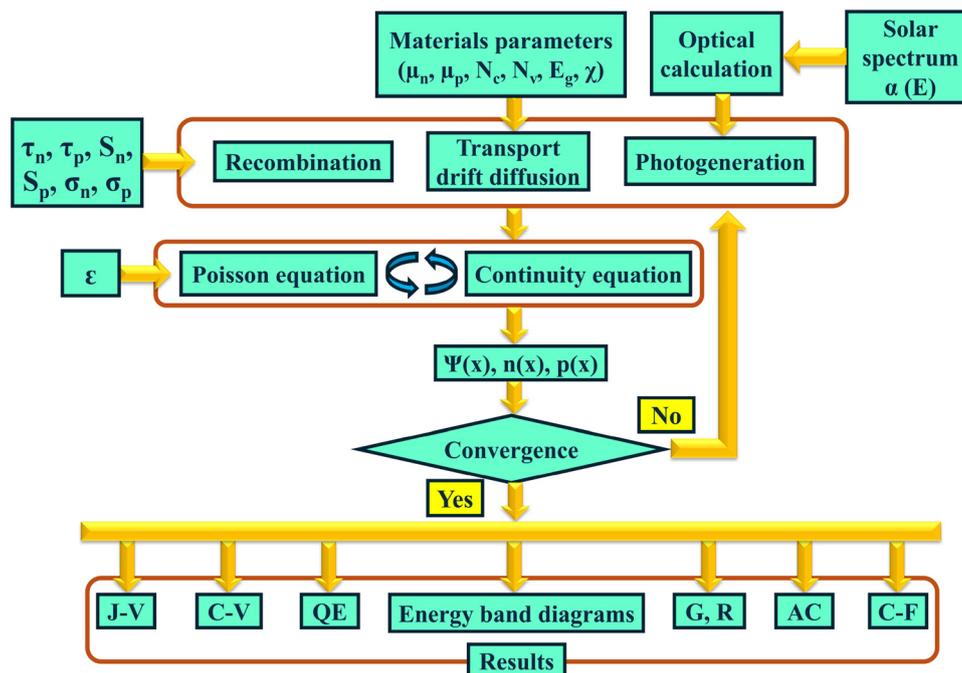
Fig. 1 SCAPS-1D simulation workflow.

Table 1 Data table of input parameters used for ITO, ETLs, and $K_2NaInBr_6$ (absorber layer)

| Parameter (unit) | ITO[57–59] | ETLs | | | | $K_2NaInBr_6$ |
		LBSO[58,60]	SnS_2[58–60]	TiO_2[57]	ZnO[57–59]	
Thickness (nm)	500	120	150	30	50	600
Bandgap, E_g (eV)	3.5	3.12	1.85	3.2	3.3	1.895
Electron affinity, X (eV)	4	4.4	4.26	3.9	4	4.025
Relative dielectric permittivity, ε_r	9	22	17.7	9	9	5.638
CB effective density of states, N_c (cm^{-3})	2.2×10^{18}	1.8×10^{20}	7.32×10^{18}	2×10^{18}	3.7×10^{18}	2.263×10^{16}
VB effective density of states, N_v (cm^{-3})	1.8×10^{19}	1.8×10^{20}	10^{19}	1.8×10^{19}	1.8×10^{19}	8.095×10^{17}
Electron thermal velocity ($cm\ s^{-1}$)	10^7	10^7	10^7	10^7	10^7	10^7
Hole thermal velocity ($cm\ s^{-1}$)	10^7	10^7	10^7	10^7	10^7	10^7
Electron mobility, μ_n ($cm^2\ V^{-1}\ s^{-1}$)	20	0.69	50	20	100	189.9
Hole mobility, μ_h ($cm^2\ V^{-1}\ s^{-1}$)	10	0.69	25	10	25	17.50
Shallow uniform donor density, N_D (cm^{-3})	10^{21}	2×10^{21}	9.85×10^{19}	9×10^{16}	10^{18}	0
Shallow uniform acceptor density, N_A (cm^{-3})	0	0	0	0	0	1×10^{15}
Defect density, N_t (cm^{-3})	10^{15}	10^{14}	10^{14}	10^{15}	10^{15}	10^{15}

Table 2 Data table of input parameters for HTLs

Parameter (unit)	CBTS[58,59,61]	Cu_2O[58,59,61]	CuI[58,59,61]	CdTe[58,60]	Cu_2Te[59,60]	Spiro_MeOTAD[58,61]
Thickness (nm)	100	50	100	200	250	200
Bandgap (eV)	1.9	2.2	3.1	1.5	1.18	3
Electron affinity (eV)	3.6	3.4	2.1	3.9	4.2	2.2
Dielectric permittivity (relative)	5.4	7.5	6.5	9.4	10	3
CB effective density of states (cm^{-3})	2.2×10^{18}	2×10^{19}	2.8×10^{19}	8×10^{17}	7.8×10^{17}	2.2×10^{18}
VB effective density of states (cm^{-3})	1.8×10^{19}	10^{19}	10^{19}	1.8×10^{19}	1.6×10^{19}	1.8×10^{19}
Electron thermal velocity ($cm\ s^{-1}$)	10^7	10^7	10^7	10^7	10^7	10^7
Hole thermal velocity ($cm\ s^{-1}$)	10^7	10^7	10^7	10^7	10^7	10^7
Electron mobility, μ_n ($cm^2\ V^{-1}\ s^{-1}$)	30	200	100	3.2×10^2	500	2.1×10^{-3}
Hole mobility, μ_h ($cm^2\ V^{-1}\ s^{-1}$)	10	8600	43.9	4×10^1	100	2.16×10^{-3}
Shallow uniform donor density, N_D (cm^{-3})	0	0	0	0	0	0
Shallow uniform acceptor density, N_A (cm^{-3})	10^{18}	10^{18}	10^{18}	2.0×10^{14}	10^{21}	10^{18}
Defect density, N_t (cm^{-3})	10^{15}	10^{15}	10^{15}	10^{15}	10^{14}	10^{15}

Table 3 Data table of interfacial properties employed in the $K_2NaInBr_6$-based PSC[58,62]

Interface	Type of defect	Capture cross-section: electrons/holes (cm^2)	Energetic distribution	Reference for defect energy levels, E_t	Total density (cm^{-2})
ETL/$K_2NaInBr_6$	Neutral	10^{-17} 10^{-18}	Single	Above the VB maximum	10^{10}
$K_2NaInBr_6$/HTL	Neutral	10^{-18} 10^{-19}	Single	Above the VB maximum	10^{10}

DFT-derived material parameters into SCAPS, it becomes possible to achieve a more realistic simulation of solar cell performance, linking theoretical material design with practical device applications. This integrated approach enables the optimization of material choices, layer thicknesses, doping concentrations, and interface engineering. The synergy between DFT and SCAPS thus enhances the overall predictive power of simulations and supports the development of more efficient and stable solar cells.

2.4 Device structure and band alignment between several ETLs and HTLs for the $K_2NaInBr_6$ absorber

Fig. 1 illustrates the simulation framework adopted in SCAPS-1D, while Fig. 2a presents the schematic of the device architecture. The proposed double perovskite solar cell (DPSC) is designed with a sequence of HTLs, ETLs, and back-contact layers, where the absorber is $K_2NaInBr_6$, arranged in an n–i–p configuration with the absorber as the intrinsic layer. In this configuration, the depletion region penetrates deeply into the intrinsic layer, enabling enhanced sensitivity to longer-wavelength photons compared to conventional p–n junctions. This allows incident light to travel further within the device. Nevertheless, photocurrent generation is mainly governed by the electron–hole pairs formed within or in close proximity to the depletion region. A broader depletion region strengthens quantum efficiency by supporting efficient carrier generation and separation.
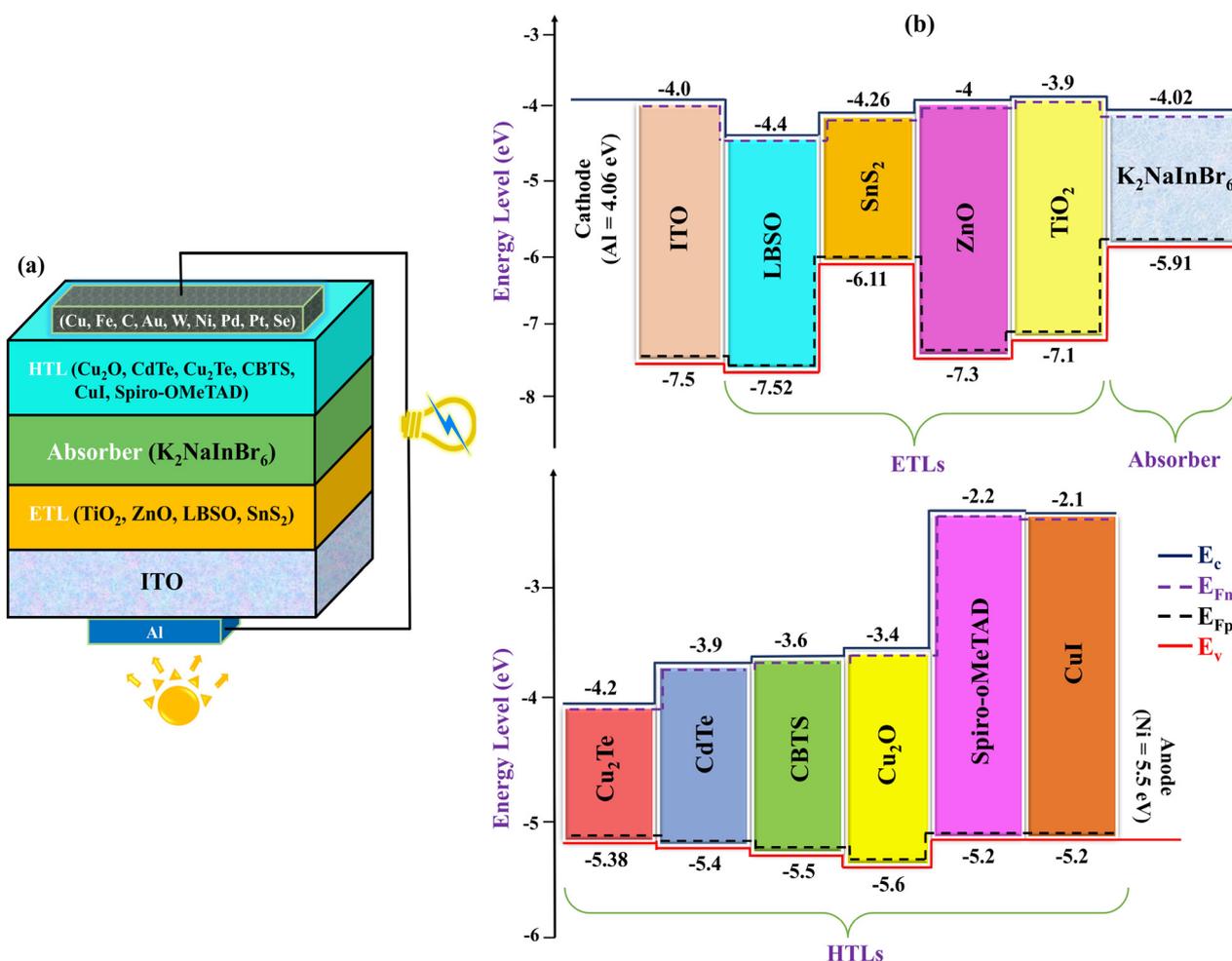
Fig. 2 (a) Device configuration. (b) Band alignment.

The double perovskite device structure of $K_2NaInBr_6$ further promotes strong light absorption. Meanwhile, the heavily doped ETL and HTL at both ends function as ohmic contacts, facilitating carrier collection and photon trapping. For this study, four ETL candidates, six HTL options, and a Ni back contact were selected based on previous reports, as summarized in Tables 1 and 2. To enhance simulation accuracy, SCAPS-1D incorporates interface defect layers, which replicate experimental interfacial imperfections; their characteristics are detailed in Table 3. This modeling approach provides a reliable platform for evaluating the performance of different DPSC configurations in terms of both electronic and optical behaviors.

Fig. 2(b) illustrates the energy band configuration in perovskite solar cells (PSCs) incorporating different electron and hole transport layers. The schematic highlights the relative positions of the conduction band (E_c) and valence band (E_v) for several electron transport layers (ETLs) such as TiO_2, ZnO, LBSO and SnS_2, when interfaced with the $K_2NaInBr_6$ absorber. Also it compares these levels with a range of hole transport layers (HTLs), including Cu_2O, CdTe, Cu_2Te, CBTS, CuI and spiro-MeOTAD alongside the nickel anode (5.5 eV). Additionally, Fig. 2(b) includes dashed lines representing the quasi-Fermi levels for electrons (E_{Fn}) and holes (E_{Fp}), which reflect carrier separation and transport behavior.

The appropriate selection of ETLs plays a crucial role in facilitating electron extraction from the perovskite layer. This process mainly depends on the conduction band offset between the ETL and the absorber; ETLs with conduction band minima nearly aligned or slightly lower than that of the absorber promote efficient electron transfer. At the same time, a relatively higher valence band edge in the ETL helps mitigate electron–hole recombination. Similarly, effective hole extraction requires close alignment between the valence band of the HTL and the valence band of the absorber, which further minimizes interfacial recombination.

2.5 Structural properties and stability

Structural analysis aids in characterizing the bandgap, bonding nature, and atomic arrangement in semiconducting and other materials.[64] Fig. 3 illustrates the relaxed crystal structure of $K_2NaInBr_6$, confirming its cubic double-perovskite framework with $Fm\bar{3}m$ space group symmetry. The optimized geometry contains 40 atoms per unit cell, equivalent to four formula units. The atomic positions are assigned as follows: K at 8c (0.25, 0.25, 0.75), Na at 4b (0.5, 0, 0), In at 4a (0, 0, 0), and Br at 24e (0.241192, 0, 0) sites, with the fractional coordinate x determined via full structural relaxation. The optimized lattice constant is 11.2912 Å, corresponding to a unit cell volume of 2428.59 Å^3.

The structural stability is assessed through three geometric indicators: the Goldschmidt tolerance factor (τ_1), the octahedral factor (μ), and the recently proposed physical tolerance factor (τ_2). These parameters are defined as:

$$\tau_1 = \frac{R_K + R_{Br}}{\sqrt{2}\left(\frac{R_K + R_{In}}{2}R_{Br}\right)} \tag{15}$$

$$\tau_2 = \frac{R_{Br}}{R_K}n_x\left(n_K - \frac{\frac{R_K}{R_{Na}}}{\ln\frac{R_K}{R_{Na}}}\right) \tag{16}$$

$$\mu = \frac{R_{Na} + R_{In}}{2R_{Br}} \tag{17}$$

Here, R_K, R_{Na}, R_{In}, and R_{Br} are the Shannon ionic radii of K^+, In^{3+} and Br^-, respectively, while n_x defines the oxidation state of K^+. For a cubic perovskite, τ_1 must be in the range of 0.813–1.107, μ must be between 0.41 and 0.89,[65] and τ_2 must be below 4.18.[66] The calculated values for $K_2NaInBr_6$ are $\tau_1 \approx 0.887$, $\mu \approx 0.464$, and $\tau_2 \approx 1.209$, as shown in Table 4, confirming that the structure resides well within the cubic stability window.

Thermodynamic stability is further examined via the formation energy (E_f) and binding energy (E_b):

$$E_f = \frac{E_{K_2NaInBr_6} - n_K \times \frac{E_K}{k} - n_{Na} \times \frac{E_{Na}}{l} - n_{In} \times \frac{E_{In}}{m} - n_{Br} \times \frac{E_{Br}}{p}}{N}$$

$$E_b = E_{K_2NaInBr_6} - n_K \times \mu_K - n_{Na} \times \mu_{Na} - n_{In} \times \mu_{In} - n_{Br} \times \mu_{Br}$$
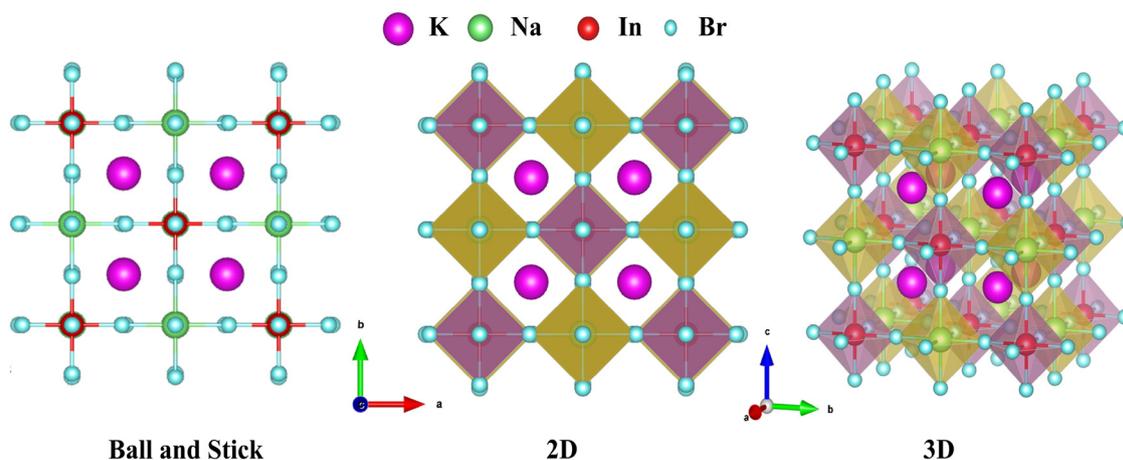

● K ● Na ● In ○ Br

Ball and Stick **2D** **3D**

Fig. 3 Crystal structure of $K_2NaInBr_6$.

Table 4 Shannon's ionic radii (r), Goldschmidt tolerance factor (τ_1), octahedral factor (μ), and new tolerance factor (τ_2) for $K_2NaInBr_6$

| DP | Ionic radius of cations (Å) | | Ionic radius of the anion (Å) | Tolerance factor (τ_1) | Octahedral factor (μ) | New tolerance factor (τ_2) |
	r_K	$(r_{Na} + r_{In})/2$	r_{Br}			
$K_2NaInBr_6$	1.64	0.91	1.96	0.887	0.464	1.209

Table 5 Bulk modulus (B_0), lattice constant (a_0), first derivative of bulk modulus (B'_0), formation energy (E_f), total energy (E_{tot}), and binding energy (E_b) for $K_2NaInBr_6$

| Compound | a_0 (Å) | B_0 (GPa) | B'_0 | E_{tot} (Ry) | | E_f (eV per atom) | | E_b (eV per atom) |
				PBE	PBEsol	PBE	PBEsol	
$K_2NaInBr_6$	11.291	21.9219	4.3033	−45 780.6379	−45 750.723	−0.0287	−0.0345	−45 780.549

where $E_{K2NaInBr6}$ is the total energy of the compound, E_K, E_{Na}, E_{In}, and E_{Br} are the atomic energies in bulk and isolated states, respectively, n is the number of atoms of each species, and N is the total number of atoms. Negative values of E_f and E_b indicate thermodynamic stability, with larger magnitudes reflecting stronger bonding.

The values of formation energy, $E_f = -0.0287$ eV per atom (PBE) and -0.0345 eV per atom (PBEsol), appear numerically small but remain physically meaningful. When expressed per formula unit, these values correspond to a substantially negative formation energy, confirming the thermodynamic stability of $K_2NaInBr_6$. Similar magnitudes of small but negative per-atom formation energies have been reported for stable lead-free halide double perovskites in a previous DFT study by Liang *et al.* for $Cs_2AgBiBr_6$ and $Cs_2AgInBr_6$.[67] And, the $E_b = -45 780.549$ eV per atom, demonstrating excellent stability and high atomic cohesion. All of the examined compounds have negative E_f and E_b values (Table 5), showing their stability. Additionally, the Birch–Murnaghan equation-of-state fitting yields a bulk modulus (B_0) of ≈ 21.9219 GPa with the pressure derivative $B'_0 \approx 4.3033$, signifying a balance between mechanical rigidity and structural flexibility, which is advantageous for photovoltaic device applications. Furthermore, Fig. 4 shows the link between minimum energy and volume for the compound under investigation.

2.6 Electronic properties

2.6.1 Band structures. The distribution of electrons across energy bands, as revealed by electronic band structures, governs a material's electrical, optical, and thermal behaviors. Insights from band structure analysis facilitate the development of advanced electronic systems such as transistors, semiconductors, and solar cells.[68] The study of a material's band structure is critical for revealing whether it exhibits conductive, semiconductive, or insulating behavior.[69] Fig. 5(a) and (b) depict the electronic band structures of $K_2NaInBr_6$ computed using PBE and PBEsol. The band structure is computed along the high-symmetry directions of the Brillouin zone, as illustrated in the figures, with the red dashed line at 0 eV representing the Fermi level (E_F). Analysis using both PBEsol and PBE functionals shows that the bands neither overlap nor
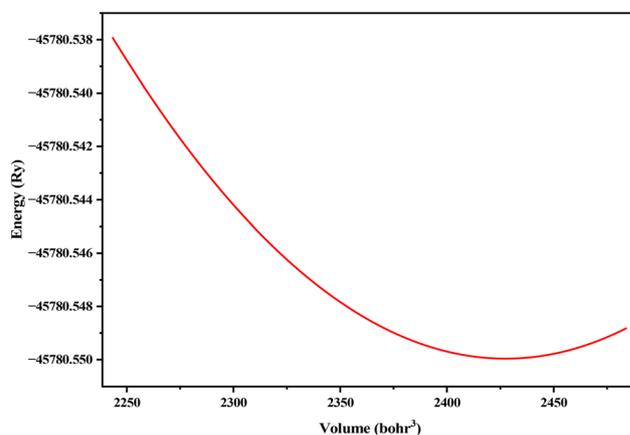
Fig. 4 Minimum energy (E) *vs.* volume (V) optimization curve.

cross the Fermi level, indicating the material's semiconducting character. According to our calculations, the CBM and VBM are aligned at the Γ point for both the functionals used. This alignment confirms the direct nature of the bandgap in $K_2NaInBr_6$, a desirable feature that enhances the effectiveness of optical transitions in semiconductor materials.[70] The band gaps for $K_2NaInBr_6$ are determined to be 1.99 eV (PBE) and 1.89 eV (PBEsol). Materials with such direct band alignment are especially beneficial for optoelectronic devices like solar cells and LEDs, where efficient photon absorption and emission are essential.[70]

2.6.2 Density of states (DOS). The total density of states (TDOS) gives a comprehensive view of the number of available electronic states at different energy levels,[71] whereas the partial density of states (PDOS) separates these contributions by specific atoms or orbitals, helping to understand bonding and hybridization. It also provides insight into the energy levels of the conduction and valence bands, emphasizing the roles of different atomic elements.[63] To gain deeper insight into the band structures, the partial and total density of states (PDOS and TDOS) for the double perovskite compound $K_2NaInBr_6$ were examined, as shown in Fig. 6. The Fermi level, indicated by a black dotted line at 0 eV, lies between the valence and conduction bands. Prominent peaks appear in the TDOS for
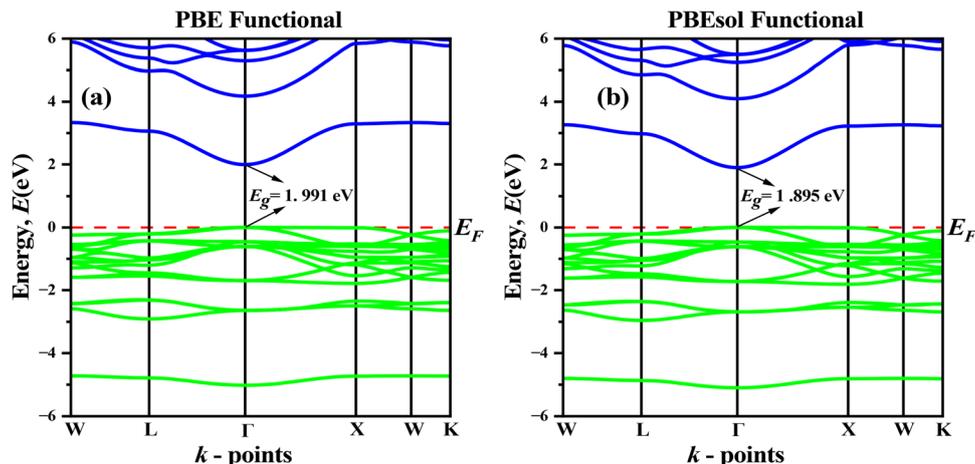
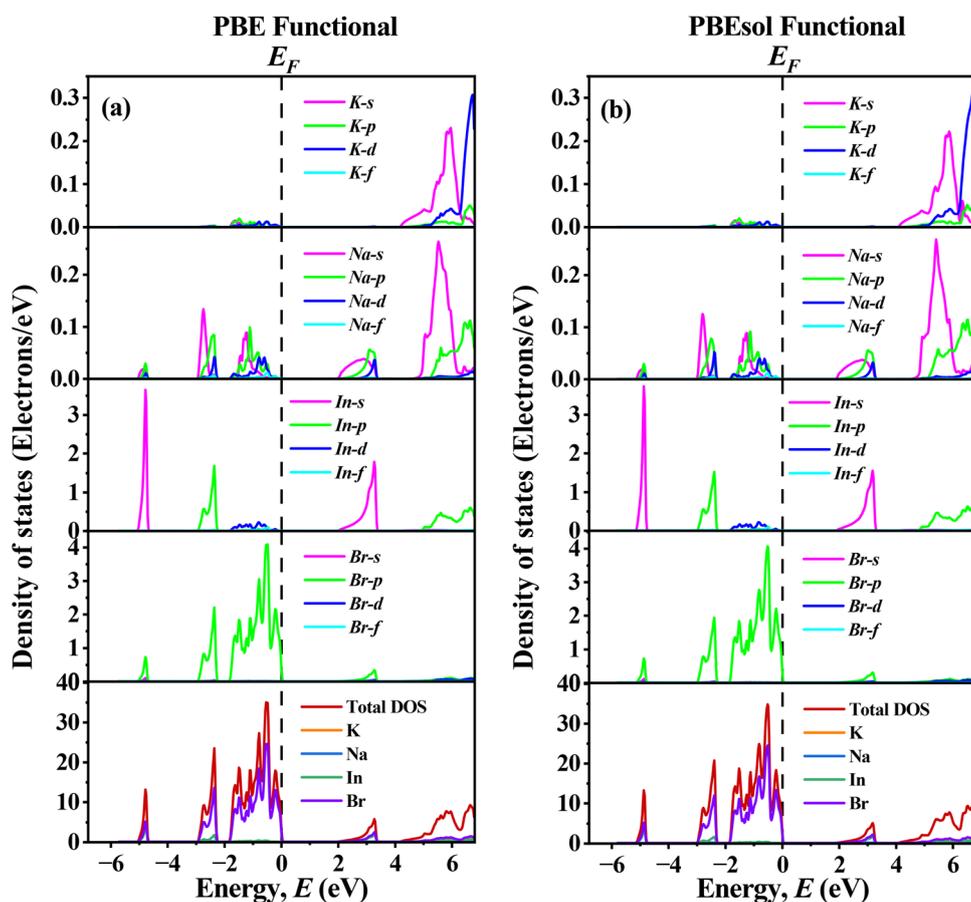**Fig. 5** Electronic band structure of $K_2NaInBr_6$ computed using (a) PBE and PBEsol (b).

Fig. 6 Total and partial density of states of $K_2NaInBr_6$ calculated using PBE (a) and PBEsol (b).

both the valence and conduction bands, suggesting a high concentration of electronic states and emphasizing the material's detailed electronic structure. The valence band is shaped mainly by the d orbitals of In and p orbitals of Br, whereas the conduction band is constructed from d orbitals of K states and s orbitals of Na and In. In the valence band, the electronic states close to the

Fermi level are primarily governed by Br-p orbitals, emphasizing their impact on the material's electronic behavior. In addition, Na-s and In-p orbitals play a limited role in shaping the valence band. In the conduction band, the K-s and Na-d orbitals show limited involvement, but their role in conduction remains significant. The coordination between these orbitals controls how electronic

transitions and conduction occur, illustrating the materials' intricate electronic behavior.

2.7 The effective mass of charge carriers and transport properties

2.7.1 Optical properties.

The investigation of optical functions provides essential insights into the electronic band structure and informs the development of advanced optoelectronic applications. The optical properties of the halide double perovskite $K_2NaInBr_6$ were systematically investigated using two computational approaches: PBE and PBEsol. The optical performance of a material is fundamentally influenced by the available electronic transitions and band gap parameters, offering a pathway to study light–matter interactions.[72] The study of optical properties has become increasingly prominent in recent decades, primarily driven by their application potential in areas such as optical information systems, modulation technologies, optoelectronics, and telecommunications.[53,73] A comprehensive set of optical parameters were evaluated, including the absorption coefficient $\alpha(\omega)$, reflectivity $R(\omega)$, refractive index $n(\omega)$, dielectric constant $\varepsilon(\omega)$, optical conductivity $\sigma(\omega)$, and loss function $L(\omega)$. These optical responses were calculated across a photon energy range of 0 to 13.55 eV, and the results are given in Fig. 7.

The photon energy-dependent absorption coefficient (α, in cm^{-1}) of $K_2NaInBr_6$ is shown in Fig. 7(a). This parameter measures the degree of light absorption by a material at different photon energies, reflecting the efficiency of photon–material interaction.[71] The material $K_2NaInBr_6$ demonstrates a noticeable rise in its absorption coefficient (α) within the visible spectrum, indicating strong photon absorption suitable for photovoltaic applications. The maximum absorption peak for $K_2NaInBr_6$ is recorded at approximately 1.37×10^5 cm^{-1} (PBE) and 140.98×10^5 cm^{-1} (PBEsol), corresponding to an energy level of about 10.43 eV, which is comparable to that of established photovoltaic absorbers such as $Cs_2AgInBr_6$ ($\sim 10^4$ cm^{-1}) and $Cs_2AgGaBr_6$ ($\sim 10^5$ cm^{-1}).[74] It is clear that the PBEsol method demonstrates a slightly greater absorption than the PBE method.

The real (σ_1) and imaginary (σ_2) components of the optical conductivity $\sigma(\omega)$ for $K_2NaInBr_6$. The real part (σ_1) of the optical conductivity remains nearly zero for photon energies below the bandgap ($\hbar\omega < E_g$), confirming the semiconducting nature of $K_2NaInBr_6$. The increase in $\sigma(\omega)$ at higher energies originates from interband electronic transitions rather than metallic free-carrier conduction. As shown in Fig. 7(b), the optical conductivity reaches its highest value at 7.27 eV calculated using the PBE and PBEsol approaches. The σ_1 values rise with increasing
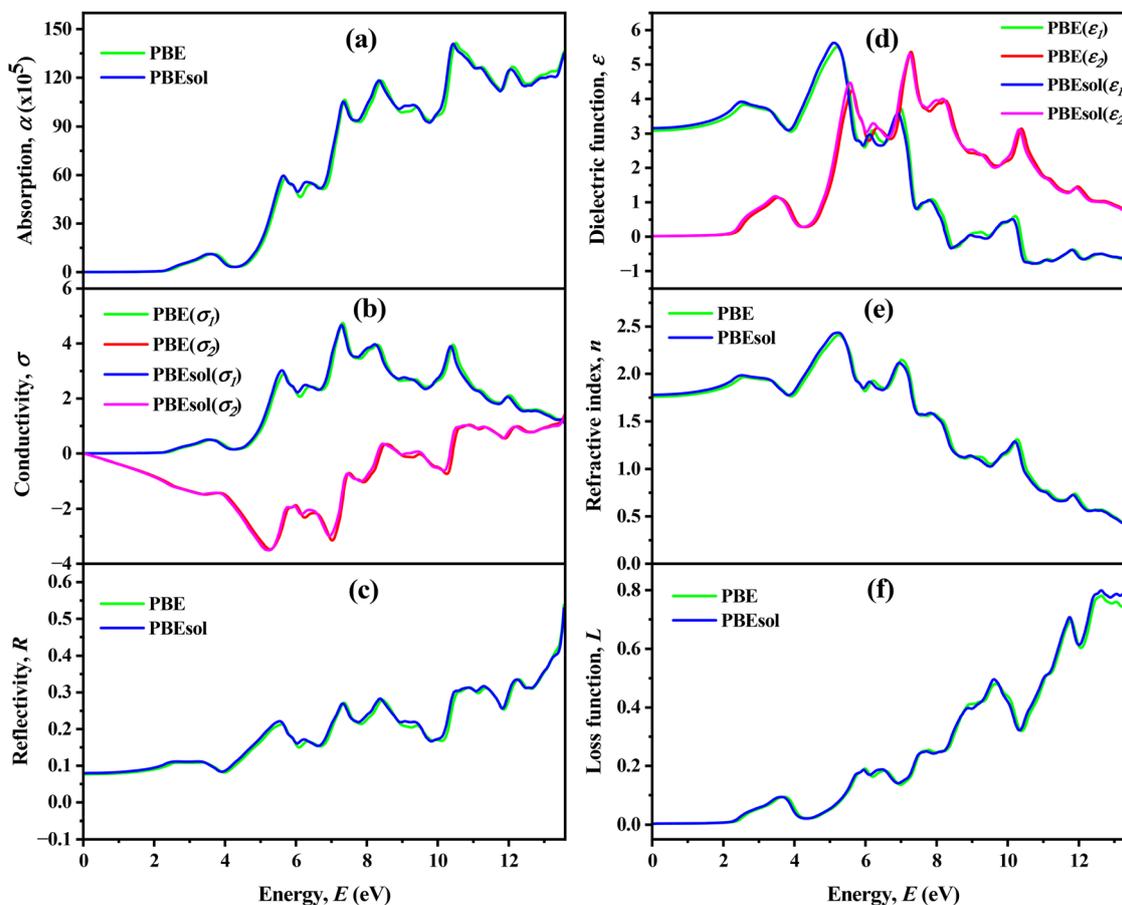

Fig. 7 Optical properties: (a) absorption, (b) conductivity, (c) reflectivity, (d) dielectric function, (e) refractive index, and (f) loss function of $K_2NaInBr_6$ based on PBE and PBEsol.

photon energy, attaining a maximum before gradually declining. In contrast, the σ_2 values decrease as energy increases, reaching a negative minimum before slowly recovering. This inverse correlation between σ_1 and σ_2 across photon energies represents photon-induced interband transitions predicted from the electronic band structure, underpinning its potential for high-performance in high-frequency photonic and optoelectronic devices.[75]

Reflectivity quantifies a material's ability to return incident radiation or light, which is a key factor in the design and performance of optical devices and energy-based systems. The reflectivity spectrum $R(\omega)$, presented in Fig. 7(c), shows minimal fluctuations in the lower energy range and a consistent upward trend at higher energies. Based on Fig. 7(c), the initial reflectivity of $K_2NaInBr_6$ is fixed at 0.07 at 0 eV for both PBE and PBEsol functionals. This compound display a progressive increase in reflectivity throughout the infrared and visible spectra. The reflectivity spectra reveal that $K_2NaInBr_6$ has peak values of 0.53 using PBE and 0.52 using PBEsol. Nonetheless, the compound $K_2NaInBr_6$ exhibits low reflectivity in the visible range, which is beneficial as it minimizes surface reflection losses and promotes efficient light absorption.[76]

The dielectric function $\varepsilon(\omega)$ is a complex, frequency-dependent parameter that characterizes how a material responds to an applied electric field, providing insight into its fundamental optical and electronic behavior. The dielectric characteristics of the $K_2NaInBr_6$ compound are evaluated through the complex dielectric constant $\varepsilon(\omega) = \varepsilon_1(\omega) + i\varepsilon_2(\omega)$ and associated optical parameters. These components are crucial for understanding light–material interactions, where the real part $\varepsilon_1(\omega)$ represents the induced polarization in the medium and the imaginary part $\varepsilon_2(\omega)$ accounts for energy loss caused by light absorption.[77] The initial values of real $\varepsilon_1(\omega)$ at 0 eV for $K_2NaInBr_6$ range from 3.08 (PBE) to 3.16 (PBEsol). The real component increases with photon energy before decreasing after attaining peak values. As shown in Fig. 7(d), the $\varepsilon_1(\omega)$ curve intersects the zero line at certain points, indicating fully reflective optical response. Our investigated compound, $K_2NaInBr_6$, exhibits the highest peak in the imaginary part of the dielectric function $\varepsilon_2(\omega)$, with values of 5.37 at 7.3 eV using PBE and 5.31 at 7.25 eV using PBEsol. These results highlight the influence of the exchange–correlation functional on optical response predictions.

A material's refractive index $n(\omega)$ defines the extent of photon refraction and reduction in speed as light passes through it, making it a critical parameter for optical applications.[78] The refractive index at zero photon energy $n(0)$ for $K_2NaInBr_6$ is calculated to be 1.75 (PBE) and 1.72 (PBEsol), as shown in Fig. 7(e). The $K_2NaInBr_6$ compound exhibits a gradual increase in the refractive index $n(\omega)$ in the visible region, while it declines at higher photon energies, indicating reduced transparency, consistent with earlier findings.[79] The refractive index of $K_2NaInBr_6$ increases with photon energy, reaching maxima of approximately 2.4 (PBE) and 2.43 (PBEsol) at 5.26 eV. After these peaks, the refractive index decreases, signifying reduced optical transparency at higher energies.

The electron energy loss function is crucial for analyzing how electrons rapidly moving through a material lose energy.[80] The loss function quantifies the energy lost by fast electrons traversing a material, where its prominent peaks mark plasmon resonance frequencies reflecting collective electron density oscillations.[70] The spectra of the loss function for $K_2NaInBr_6$ are illustrated in Fig. 7(f). Maximum values of 0.779 (PBE) and 0.79 (PBEsol) are found at 12.63 eV. As the energy increases, the loss function for the $K_2NaInBr_6$ compound also rises, indicating the presence of peaks that correspond to plasmon resonance frequencies.

2.8 Analysis of SCAPS-1D results

2.8.1 Effects of HTL and ETL layers.
In perovskite solar cells (PSCs), the electron transport layer (ETL) extracts electrons from the $K_2NaInBr_6$ absorber and transfers them to the ITO electrode, while the hole transport layer (HTL) collects holes and directs them toward the Ni back contact. Thus, proper charge extraction through the ETL and HTL is fundamental to the effective operation of PSC devices. Device performance can be optimized by simulating various ETL and HTL configurations with $K_2NaInBr_6$ as the absorber. We investigated device architectures using electron transport materials (TiO_2, ZnO, LBSO, and SnS_2) alongside multiple hole transport materials. Fig. 8 graphically illustrates the performance variations across the 24 device configurations. Evaluation of all ETM/HTM layer configurations with the $K_2NaInBr_6$ absorber and Ni contacts revealed that Cu_2O consistently delivered the best performance across all ETLs. Eight device configurations exhibited the best performance and efficiency out of the 24 possible combinations. The performance of V_{OC}, J_{SC}, FF, and PCE for these eight device combinations aligns favorably with the results in Table 6.

2.8.2 Left metal contact optimization.
In this part of the study, emphasis is placed on the optimization of the left metal contact (LMC) layer in the ITO/ETLs/$K_2NaInBr_6$/Cu_2O/LMC perovskite solar cell configuration. A total of eight distinct LMC work function variations were systematically investigated to enhance the photovoltaic output parameters. The classification of the metals was performed based on their work function values, as these strongly influence charge transport and interfacial behavior. It is well established that a lower work function in the contact metal generally leads to reduced shunt resistance (R_{sh}) and diminished device efficiency. In particular, iron (Fe) exhibited the weakest performance among the tested LMCs, not only due to its relatively low work function but also because of its pronounced stability issues, such as susceptibility to diffusion and corrosion.

Conversely, when high work function metals such as iron (Fe) are replaced with other high work function contacts, beneficial band bending occurs at the perovskite–hole transport material (HTM)–LMC interface. This band alignment acts as an effective energy barrier to prevent electron leakage from the perovskite to the metal layer, thereby enhancing R_{sh} and minimizing the alternate current leakage pathways previously caused by low R_{sh} values. Such metals also display minimal
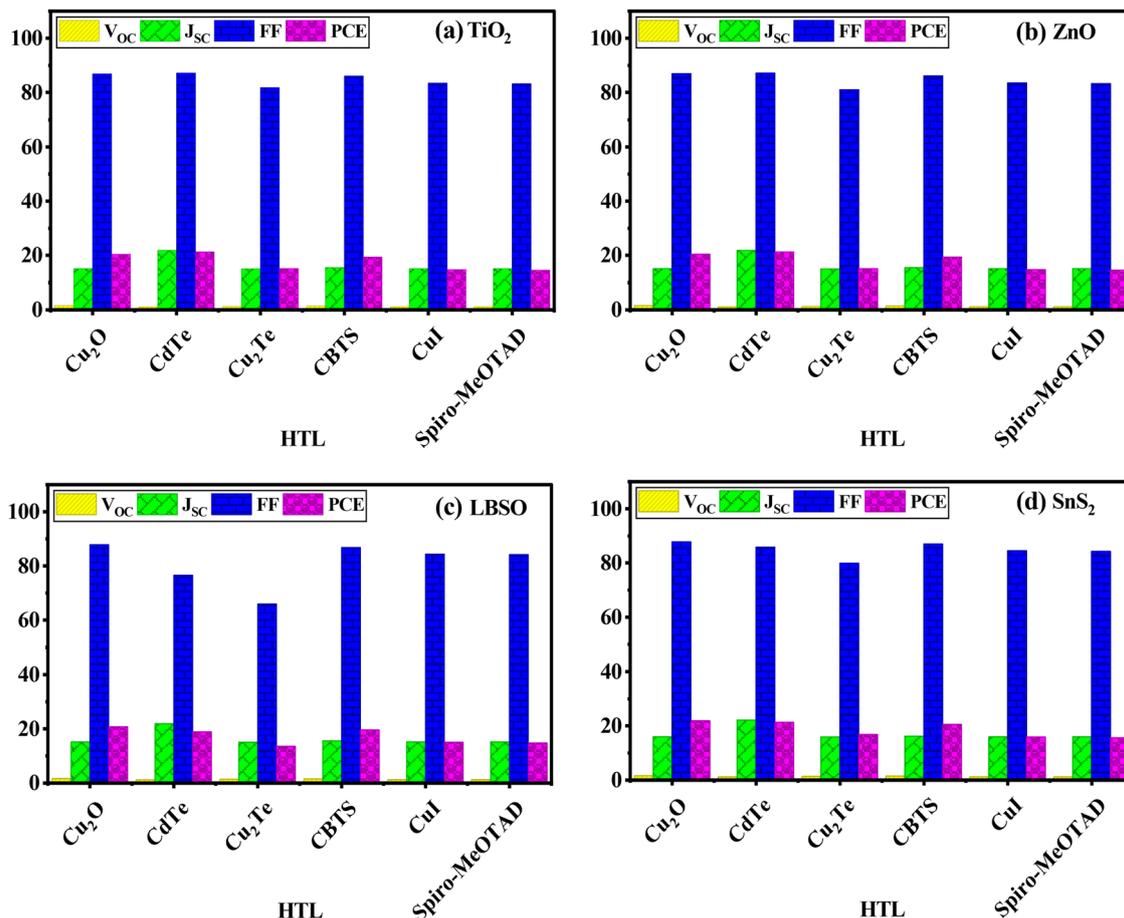
Fig. 8 Variation of performance parameters for different HTLs with Ni as the back metal contact and ETLs of (a) TiO_2, (b) ZnO, (c) LBSO, and (d) SnS_2.

Table 6 PV performance parameters of the eight device combinations

Optimized devices	V_{OC} (V)	J_{SC} (mA cm^{-2})	FF (%)	PCE (%)
ITO/ZnO/K$_2$NaInBr$_6$/Cu$_2$O/Ni	1.5565	15.094318	86.99	20.44
ITO/LBSO/K$_2$NaInBr$_6$/Cu$_2$O/Ni	1.5620	15.094806	87.80	20.70
ITO/SnS$_2$/K$_2$NaInBr$_6$/Cu$_2$O/Ni	1.5637	15.928609	87.75	21.86
ITO/TiO$_2$/K$_2$NaInBr$_6$/Cu$_2$O/Ni	1.5569	15.094243	86.88	20.42
ITO/ZnO/K$_2$NaInBr$_6$/Cu$_2$O/Ni	1.1185	21.834602	87.19	21.29
ITO/SnS$_2$/K$_2$NaInBr$_6$/CdTe/Ni	1.1232	22.080823	85.84	21.29
ITO/TiO$_2$/K$_2$NaInBr$_6$/Cu$_2$O/Ni	1.1183	21.834499	87.20	21.29
ITO/SnS$_2$/K$_2$NaInBr$_6$/CBTS/Ni	1.4586	16.158558	87.04	20.51

interfacial resistance with the HTM, facilitating efficient hole collection. Nonetheless, once the LMC work function surpasses a certain threshold, further increases do not significantly improve device performance because the alternating current leakage pathway is already eliminated, and R_{sh} has reached saturation. Additionally, a lower work function is often correlated with an improved fill factor (FF) as it reduces the reverse saturation current density, thereby boosting charge extraction efficiency.

As demonstrated in Fig. 9(a)–(d), for each ETL, selenium (Se), platinum (Pt), and palladium (Pd) achieved slightly higher performance than nickel (Ni). For example, in Fig. 9(d), for the SnS$_2$ ETL-based device, the PCE achieved when using Se, Pt, Pd,

and Ni is 21.8825%, 21.8819%, 21.8691%, and 21.8558%, respectively. Although Se, Pt, and Pd exhibit slightly higher efficiency than Ni, Ni is considerably more cost-effective compared to Se, Pt, and Pd, making it a practical alternative for large-scale manufacturing. The ITO/SnS$_2$/K$_2$NaInBr$_6$/Cu$_2$O/Ni configuration emerged as the most promising in terms of balanced performance and cost, delivering a PCE of 21.8558%, an open-circuit voltage (V_{OC}) of 1.5637 V, a short-circuit current density (J_{SC}) of 15.9286 mA cm^{-2}, and an FF of 87.7494%.

To ensure effective hole extraction through the LMC, establishing an ohmic contact is essential.[81] In this work, aluminum (Al) with a work function of 4.06 eV was utilized as the counter contact.[82] The work function values for the eight LMC metals studied – Fe, carbon (C), Au, tungsten (W), Ni, palladium (Pd), Pt, and selenium (Se) –were 4.81, 5.00, 5.10, 5.22, 5.50, 5.60, 5.70, and 5.90 eV, respectively.[59,82,83] The initial simulation employed Au as the LMC; however, subsequent adjustments in the LMC material revealed pronounced variations in device characteristics in the energy band diagrams, primarily attributed to the formation and modulation of the Schottky barrier at the interface.

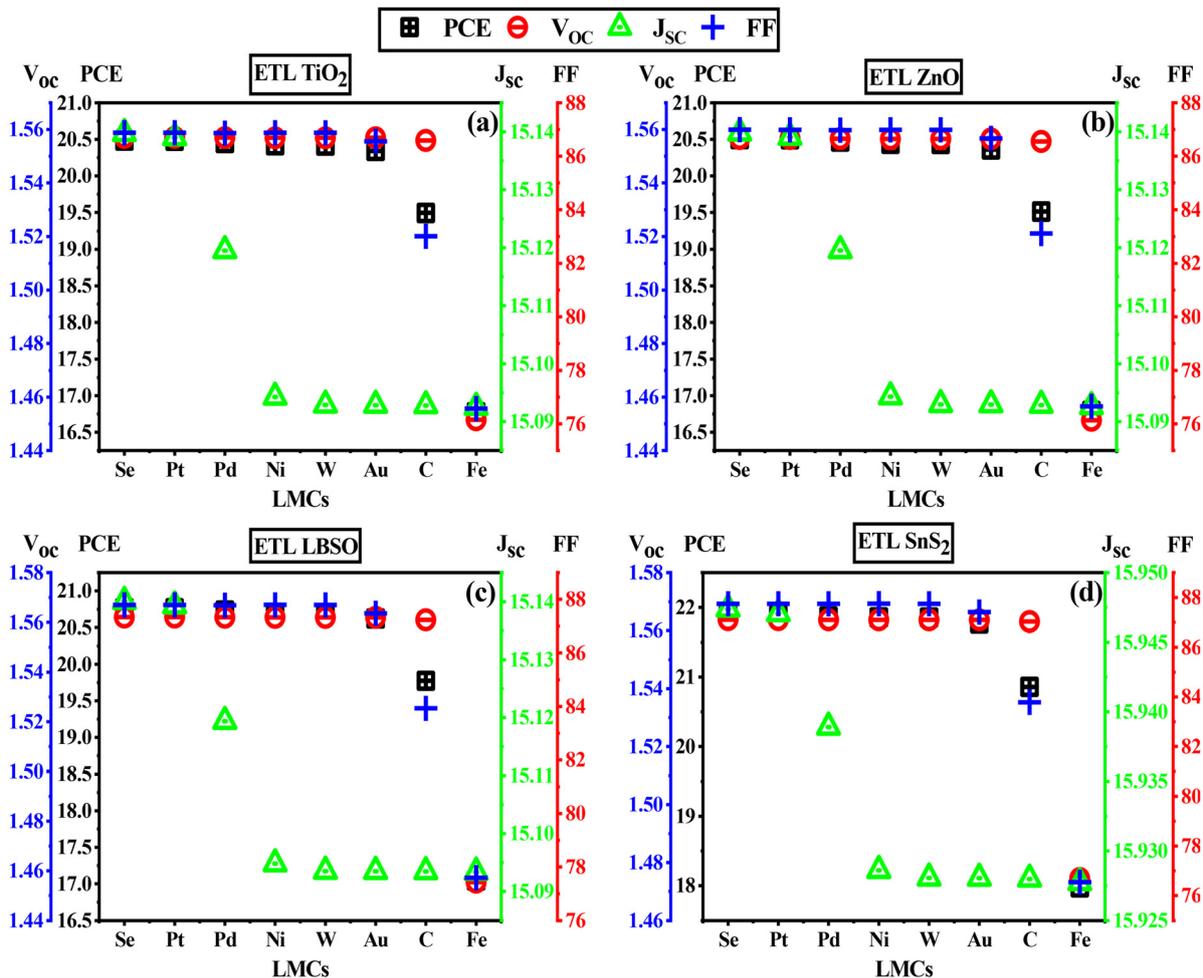**2.8.3 Band diagram.** The energy band diagram corresponding to the four optimized K$_2$NaInBr$_6$ double halide

Fig. 9 Influence of various LMCs in the structure of ITO/ETL/$K_2NaInBr_6$/Cu_2O/LMCs, where (a) Ti_2O, (b) ZnO, (c) LBSO, and (d) SnS_2 are used as ETLs.

perovskites is displayed in Fig. 10. The energy band diagram illustrates the band gap and thickness of each material within the structures. The quasi-Fermi levels, F_n and F_p, for each device coexist with the corresponding conduction band (E_c) and valence band (E_v) energies, as shown in Fig. 10(a)–(d). In every ETL, F_p appeared above E_v, whereas F_n and E_c maintained their harmonic relationship. The alignment of energy levels significantly influences the efficiency and performance of perovskite solar cells (PSCs). The ETL-generated holes in PSCs are transferred to the HTL, while light-induced electrons are directed toward the ITO and Ni back contact. To facilitate electron movement to the absorber–ETL interface, the ETL should possess greater electron affinity than $K_2NaInBr_6$. Similarly, the HTL must have an ionization energy lower than that of $K_2NaInBr_6$, since proper energy-level alignment, achieved by minimizing the interface gap between the two materials, significantly influences PSC efficiency and performance.

2.8.4 Impact of valence band offset (VBO) and conduction band offset (CBO). The ETL and HTL play a crucial role in transferring charge carriers to the respective electrodes, thereby improving the overall PCE of PSCs. In addition to charge extraction, these transport layers act as selective barriers that

suppress interfacial charge recombination by regulating the movement of unwanted carriers, namely electrons at the HTL side and holes at the ETL side. The perovskite absorber, when illuminated, generates electron–hole pairs, and the efficiency of separating these photogenerated carriers is largely determined by the band alignment at the absorber/ETL and absorber/HTL junctions. This alignment is quantified through conduction band offset (CBO) and valence band offset (VBO), which directly influence interfacial charge transfer dynamics and, consequently, device performance.[84]

The CBO at the ETL/absorber interface is mathematically defined as:[85]

$$CBO = \chi_{Absorber} - \chi_{ETL} \qquad (18)$$

where $\chi_{Absorber}$ and χ_{ETL} denote the electron affinities of the absorber and ETL layers, respectively. Based on the CBO values, three types of band alignments can occur: (1) flat barrier: observed when the CBO is nearly zero, indicating negligible energy difference, leading to unhindered electron transport; (2) cliff-like barrier: formed when the CBO is negative (χ_{ETL} > $\chi_{Absorber}$), which enhances interfacial recombination and reduces device efficiency; and (3) spike-like barrier: observed

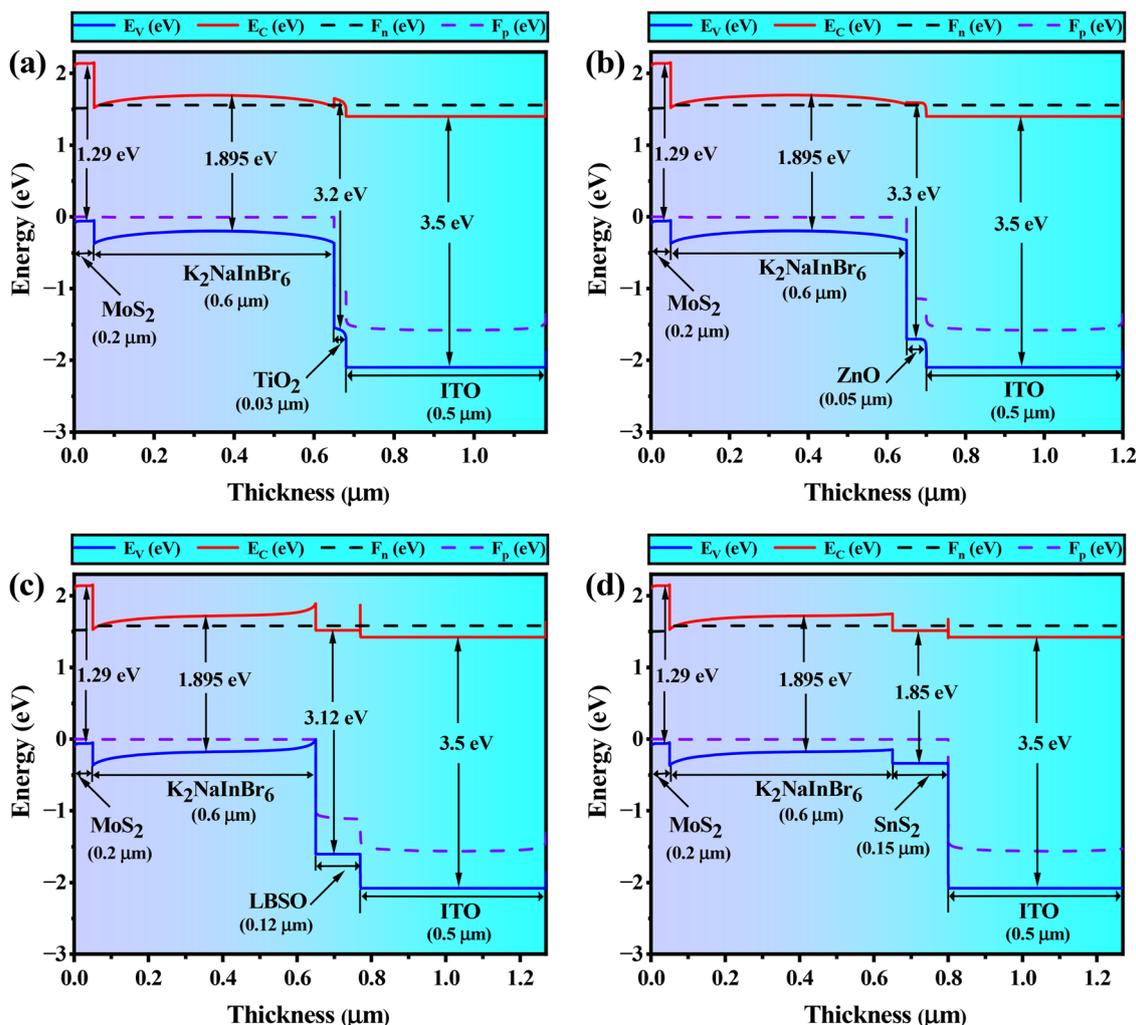**Fig. 10** Energy band diagram of $K_2NaInBr_6$.

when the CBO is positive ($\chi_{ETL} < \chi_{Absorber}$), where a potential barrier exists but can facilitate carrier selectivity if moderate in magnitude.[86]

Similarly, the VBO at the absorber/HTL interface can be expressed as eqn (19).[87]

$$VBO = \chi_{HTL} - \chi_{Absorber} + E_{g,HTL} - E_{g,Absorber} \quad (19)$$

Here, VBO represents the valence band offset and the χ_{HTL} and $\chi_{Absorber}$ are the electron affinities of the HTL and absorber. $E_{g,HTL}$ and $E_{g,Absorber}$ correspond to the bandgaps of the HTL and absorber, respectively. Appropriate alignment ensures efficient hole extraction while minimizing the probability of back-transfer of electrons.

For illustration, considering SnS_2 as the ETL paired with the double perovskite $K_2NaInBr_6$, the CBO is determined as: CBO = 4.025–4.26 eV = −0.235 eV. This negative value corresponds to a cliff-like barrier, which is moderately beneficial for reducing electron back-injection from ZnO to the absorber. On the other hand, the corresponding VBO for the absorber/HTL junction is obtained as: VBO = 3.4–4.025 eV + 2.2–1.895 eV = −0.32 eV.

Such a negative offset reflects a cliff-like barrier, which may obstruct hole transport and potentially lower FF and V_{OC}. These findings highlight that careful tuning of band offsets is necessary for balancing charge selectivity and minimizing recombination pathways.

Table 7 summarizes the comparative CBO and VBO values for the absorber with four distinct ETLs, showing distinct barrier types that can either enhance or deteriorate device efficiency depending on their sign and magnitude.

2.8.5 Impact of absorber and ETL thickness on cell performance. The photovoltaic characteristics of solar cells can be significantly improved by optimizing the absorber and ETL layer thicknesses, which are essential for maximum efficiency.[63,88] This section presents a 3D contour analysis to explore the influence of the $K_2NaInBr_6$ absorber and selected ETL thicknesses on PSC performance. Selecting an appropriate absorber and ETL thickness combination is key to developing efficient solar cells.

The study utilized TiO_2, ZnO, LBSO, and SnS_2 as ETLs, $K_2NaInBr_6$ as the absorber layer, and Cu_2O as the HTL.

Table 7 Comparative CBO and VBO values of several ETL materials with the absorber

Absorber	ETLs Four ETLs	CBO Values	CBO Comment (barrier)	VBO Values	VBO Comment (barrier)
$K_2NaInBr_6$	TiO_2	0.125	Spike-like	−0.32	Cliff-like
	ZnO	0.025			
	LBSO	−0.375	Cliff-like		
	SnS_2	−0.235			

The influence of the four optimized PSCs on photovoltaic metrics (V_{OC}, J_{SC}, FF, and PCE) was analyzed using 3D contour maps, varying absorber thickness between 0.3 and 0.7 μm and ETL thickness from 0.05 to 0.25 μm during simulations, as presented in Fig. S1–S4.

Fig. S1(a)–(d) illustrates 3D contour graphs that evaluate the impact of varying the thickness of the $K_2NaInBr_6$ absorber and ETL on the V_{OC} of the solar cells analyzed. According to Fig. S1(d), the SnS_2 PSC achieved the peak V_{OC} of approximately 1.572 V; when the V_{OC} peaks, the absorber thickness varies between 0.3 and 0.35 μm and the ETL thickness is in the 0.20 to 0.25 μm range. Among the analyzed configurations, the LBSO ETL device exhibited the lowest V_{OC} value of 1.563 V, corresponding to absorber thicknesses from 0.38 to 0.5 μm and ETL thicknesses from 0.05 to 0.25 μm, as shown in Fig. S1(c).

The impact of absorber and ETL thickness variations on the short-circuit current density (J_{SC}) of the evaluated solar cells is shown in Fig. S2, where the SnS_2 ETL device achieves the highest J_{SC} of 16.50 mA cm^{-2} (Fig. S2d). This peak occurs when the absorber thickness is approximately 0.6 to 0.7 μm and the ETL thickness is about 0.16 to 0.25 μm for SnS_2. In contrast, configurations with TiO_2, ZnO, and LBSO ETLs exhibit a minimum J_{SC} near 15.55 mA cm^{-2} at absorber thicknesses of 0.6–0.7 μm and ETL thicknesses between 0.05 and 0.25 μm, as shown in Fig. S2(a)–(c). Increasing absorber thickness leads to higher J_{SC} values across all cells, as the spectral response improves in the longer wavelength range.[61]

The effect of absorber and ETL thickness variations on FF is illustrated through 3D contour plots in Fig. S3. Notably, the TiO_2 ETL-based device in Fig. S3(a) reached a peak FF of 89.71% at absorber thicknesses between 0.3 and 0.35 μm and ETL thicknesses of 0.05 to 0.25 μm. The lowest FF value of 87.99% was observed in solar cells with the SnS_2 ETL as shown in Fig. S3(d). It is also noteworthy that ETL thickness was not a determining factor for achieving the highest FF among the four designs.[89]

The effects of altering absorber and ETL thicknesses on power conversion efficiency in various solar cells are depicted in the 3D contour maps shown in Fig. S4. Among the four optimized configurations, the solar cell with the SnS_2 ETL and the Cu_2O HTL achieved the highest PCE of approximately 22.68%, occurring with absorber thicknesses between 0.6 and 0.7 μm and ETL thicknesses from 0.16 to 0.25 μm, as depicted in Fig. S4(d). However, the ETL (TiO_2)/HTL (Cu_2O) solar configuration exhibited the lowest optimized PCE of about 21.20%, when the absorber layer thickness was between 0.65 and 0.7 μm and the ETL thickness ranged from around 0.05 to 0.25 μm, as depicted in Fig. S4(a).

2.8.6 Impact of absorber layer thickness and defect density on cell performance for $K_2NaInBr_6$. The solar cell's efficiency is strongly influenced by both the thickness of the absorber layer and its defect density (N_t). This section explores the combined influence of defect density (N_t) and absorber thickness on a $K_2NaInBr_6$ absorber-based solar cell. The statistical importance of these effects is shown in Fig. S5–S11. The PV characteristics of four optimized PSCs were simulated by varying absorber thickness (0.3–0.7 μm) and defect density N_t (1×10^{13}–1×10^{18} cm^{-3}) to assess their combined influence, as presented in Fig. S5–S11.

Fig. S5 illustrates how the open-circuit voltage (V_{OC}) varies with absorber thickness and defect density (N_t) in solar cells using ETLs (TiO_2, ZnO, LBSO, and SnS_2) combined with MoS_2 as the HTL. According to Fig. S5(a)–(c), for absorber thicknesses between 0.35 and 0.7 μm and N_t ranging from 1×10^{13} to $<1 \times 10^{17}$ cm^{-3}, TiO_2, ZnO, and LBSO ETL devices record the lowest V_{OC} close to 1.58 V. As depicted in Fig. S5(d), SnS_2 ETL solar cells show a minimum V_{OC} near 1.59 V with defect densities ranging from 1×10^{13} to 1×10^{15} cm^{-3} and absorber thickness between 0.3 and 0.7 μm.

The SnS_2 ETL solar cell shows superior J_{SC} performance, reaching up to 16.20 mA cm^{-2} (Fig. S6d), when the absorber thickness lies between 0.6 and 0.7 μm and N_t is approximately 1.0×10^{13} to 1.0×10^{16} cm^{-3}. In contrast, TiO_2-, ZnO-, and LBSO-based devices show lower J_{SC} values, around 15.55 mA cm^{-2} (Fig. S6(a)–(c)), due to insufficient photon absorption in the perovskite absorber layer, which negatively impacts overall efficiency.

The maximum fill factor of 90.10% is recorded in TiO_2 and ZnO ETL solar cells when the absorber thickness is between 0.3 and 0.4 μm and defect density ranges from 1.0×10^{13} to 1.0×10^{14} cm^{-3}, according to Fig. 11(a) and (b). Fig. 11(c) and (d) demonstrates that the FF of PSCs peaks at an N_t of around 1.0×10^{13} to 1.0×10^{14} cm^{-3} and the absorber thickness ranging from 0.3 to 0.4 μm for LBSO and SnS_2 ETL based solar cells, achieving the lowest FF of ≈89.90%. The reduction in fill factor as the absorber thickness increases is likely due to higher series resistance, reduced carrier diffusion length, and increased internal power losses within the thicker absorber layer.[90]

The overall influence of absorber thickness and defect density on power conversion efficiency (PCE) is displayed in Fig. 12(d), where the SnS_2-based ETL achieves a peak PCE of 23.10% at absorber thicknesses of 0.6–0.7 μm and N_t values of nearly 1.0×10^{13} to 1.0×10^{14} cm^{-3}. For the same absorber thickness and N_t values, the TiO_2 and ZnO ETL devices (Fig. 12(a) and (b)) reach 22.15% efficiency, while the LBSO ETL device (Fig. 12c) shows a reduced efficiency of 21.95%. Previous findings reveal that increasing defect density within the perovskite layer leads to a notable reduction in carrier diffusion length, negatively impacting the device efficiency.[91] Consequently, we selected a lower defect density for our study material.
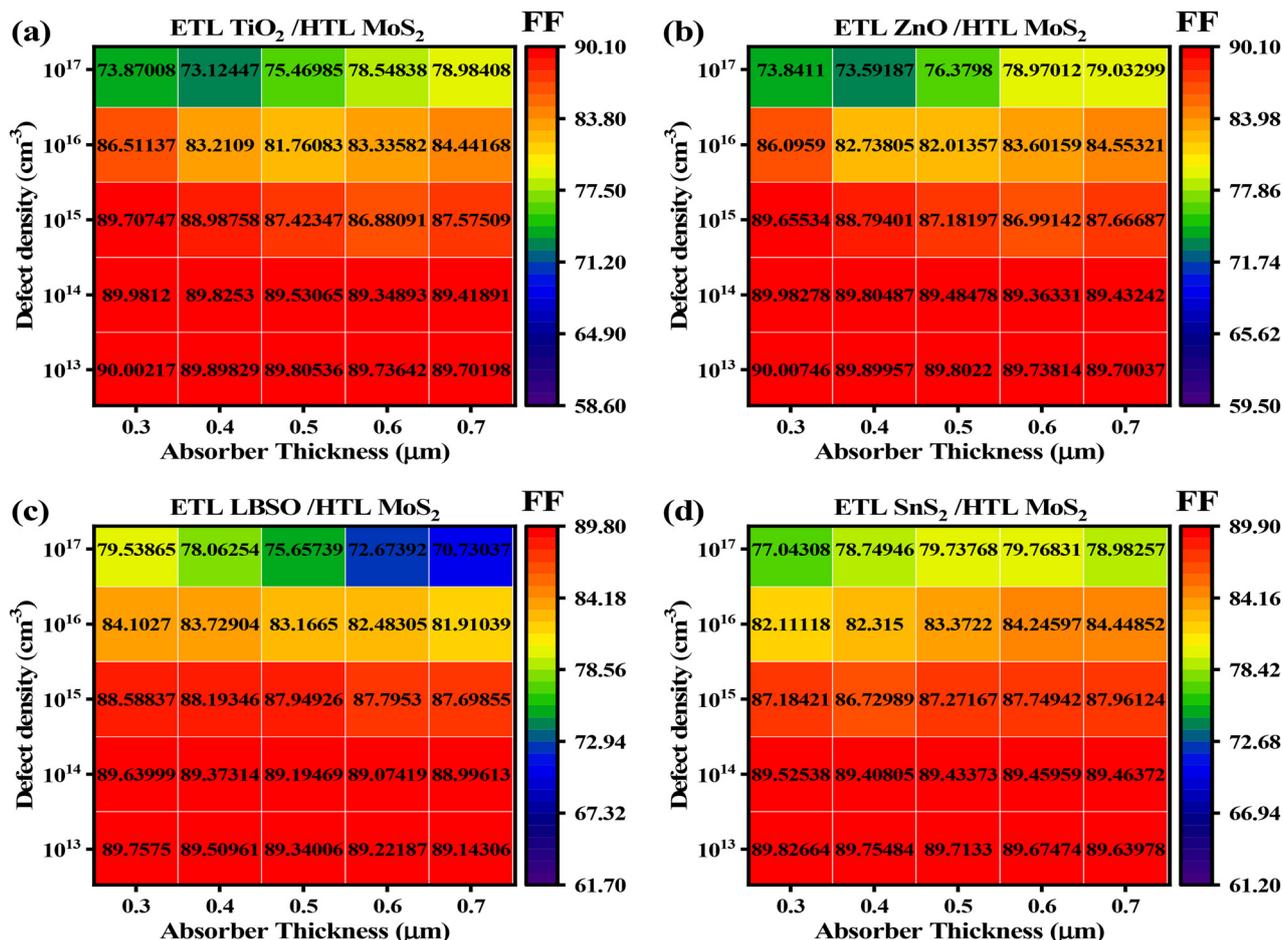
Fig. 11 Effect of the variation in absorber thickness and defect density on FF, where (a) Ti₂O, (b) ZnO, (c) LBSO, and (d) SnS₂ are used as ETLs.

2.8.7 Effect of series resistance. Series resistance plays a significant role in determining the performance of a solar cell, as it directly affects the current flow and power output under illumination. This resistance mainly arises from the interfaces between various layers of the solar cell, the metal contacts on either side, and defects introduced during the fabrication process.[88] The performance of the solar cell is highly dependent on the interaction of these factors.[57] Fig. S7 demonstrates that the series resistance (R_s) of ITO/ETL/K₂NaInBr₆/MoS₂/Ni structures fluctuated within the range of 1 to 6 Ω cm². The open-circuit voltage (V_{OC}) and short-circuit current density (J_{SC}) exhibited nearly consistent behavior regardless of changes in series resistance (R_s) in ETL-based devices. The rise in series resistance (R_s) caused a considerable decrease in FF and PCE, mirroring the results obtained for various types of solar cells, including inorganic and organic.[57,92,93] Fig. S7 reveals that the SnS₂ ETL based device exhibited the highest V_{OC} and J_{SC} among all ETL configurations. The SnS₂ ETL-based device attained peak V_{OC} and J_{SC} values of approximately 1.5635 V and 15.9 mA cm⁻², respectively, according to the figure. Regarding the fill factor, LBSO and SnS₂ ETL based devices performed almost identically under varying series resistance, and this trend was likewise observed for TiO₂ and ZnO ETL

based devices. The figure demonstrates that the SnS₂ ETL based device achieves a PCE of approximately 22%, the highest among the devices studied. It is evident that minimizing the series resistance (R_s) helps reduce its impact on power conversion efficiency (PCE) and fill factor (FF), thereby enhancing the overall solar cell efficiency.

2.8.8 Effect of shunt resistance. Shunt resistance (R_{sh}) in photovoltaic devices provides an unintended pathway for current leakage, bypassing the load and resulting in reduced output power and overall device efficiency.[94] To evaluate the influence of R_{sh} on device performance, values between 10^1 and 10^7 Ω cm² were examined, with R_s maintained constant across all three optimized solar cell configurations. The corresponding variations in V_{OC}, J_{SC}, FF, and PCE are shown in Fig. S8. The Shockley equation, shown in eqn (20) and (21), models the expected J–V behavior of a solar cell under ideal one-sun conditions:[95]

$$J_{SC} = J_{PH} - J_0 \left[\exp\left(\frac{q_e(V - JR_s)}{nkT_e} \right) - 1 \right] - \frac{V - JR_s}{R_{sh}} \quad (20)$$

$$V_{OC} = \left(\frac{nkT_e}{q_e} \right) \ln \left\{ \frac{J_{PH}}{J_0} \left(1 - \frac{V_{OC}}{J_{PH}R_{sh}} \right) \right\} \quad (21)$$
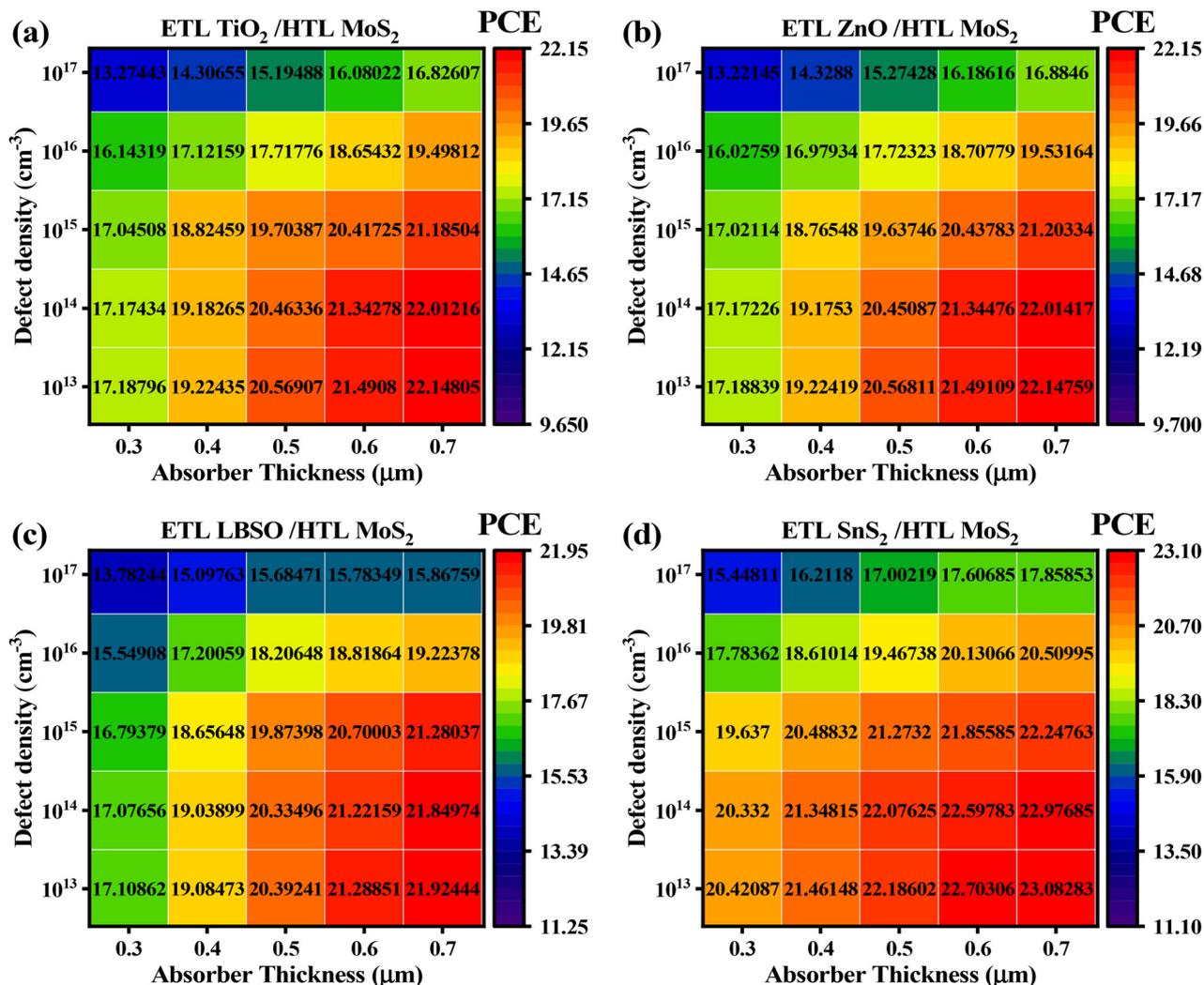
Fig. 12 Effect of the variation in absorber thickness and defect density on PCE, where (a) Ti_2O, (b) ZnO, (c) LBSO, and (d) SnS_2 are used as ETLs.

Here, q_e represents the elementary charge; J_{PH} denotes the photocurrent density; J_0 is the reverse saturation current density; R_s and R_{sh} correspond to the series and shunt resistances, respectively; n is the diode ideality factor; k is the Boltzmann constant $(1.38 \times 10^{-23}$ J K$^{-1})$; and T_e is the ambient temperature, taken as 298 K.

To maintain maximum performance, it is important to minimize localized shunting and current leakage.[96] In Fig. S8(a), V_{OC} rises up to 10^2 Ω cm^2, after which it stabilizes and shows negligible changes for R_{sh} values exceeding 10^3 Ω cm^2. A similar trend is observed for J_{SC} in Fig. S8(b). PCE and FF show an upward trend with R_{sh} reaching 10^3 Ω cm^2 in Fig. S8(c) and (d), beyond which they maintain consistent values. Optimal performance is achieved by minimizing R_{sh} and maximizing R_s.[97]

2.8.9 Impact of temperature. The temperature of a working solar cell typically exceeds the ambient level, leading to a noticeable drop in PV performance. To study this phenomenon, the temperature range was varied between 270 K and 470 K, with the resulting effects on PV parameters (V_{OC}, J_{SC}, FF, and PCE) shown in Fig. S9. The results show that J_{SC} is mostly

unaffected by temperature increase, whereas V_{OC}, FF, and PCE decline. This indicates that higher temperatures boost carrier thermal mobility in the device. At higher operating temperatures, the absorber can begin to conduct like a resistor, slowing charge movement and turning some generated electricity into heat, which lowers FF, V_{OC}, and PCE.[83,98] Over the temperature range of 270 K to 470 K, the PCE of the TiO_2 ETL-based device drops from 20.93% to 16.28% and for the ZnO ETL-based device from 20.96% to 16.29%, the LBSO ETL-based device from 20.79% to 16.69%, and the SnS_2 ETL-based device from 22.40% to 17.28%. Among all ETLs, SnS_2 consistently delivered the highest efficiency across the temperature range, demonstrating excellent thermal stability and strong potential for high-performance solar cells in diverse climates. The J_{SC} values for TiO_2, ZnO, and LBSO remained almost unchanged, implying stable photon absorption and carrier production; in contrast, SnS_2 consistently achieved ~16 mA cm^{-2}, pointing to enhanced transport and optical absorption. The study shows that the SnS_2 based ETL provides the best FF performance, beginning near 88.99%, while the TiO_2 ETL yields the lowest FF

readings in comparison. The rise in temperature alters the diffusion length and series resistance, leading to quick variations in FF and PCE.[99,100] The measured V_{OC} reduces from 1.57 V to 1.34 V for TiO$_2$ and ZnO ETLs, from 1.57 V to 1.35 V for the LBSO ETL, and from 1.58 V to 1.34 V for the SnS$_2$ ETL. All four materials (TiO$_2$, ZnO, LBSO, and SnS$_2$) showed a noticeable drop in V_{OC} with rising temperature, mainly caused by increased carrier recombination at elevated thermal energies. For all optimized devices, V_{OC} declines with increasing temperature because it is inversely related to J_0, which increases with temperature, as expressed in eqn (22):

$$V_{OC} = \frac{AK'T_1}{q}\left[\ln\left(1 + \frac{J_{SC}}{J_0}\right)\right] \quad (22)$$

where $\frac{K'T_1}{q}$ denotes the thermal voltage. A rise in PSC temperature enhances defect presence, leading to reduced V_{OC}, as observed in earlier research.[57] It is demonstrated by the equation that higher temperatures raise J_0, which reduces V_{OC}.

2.8.10 Effects of capacitance and Mott–Schottky (MS) analysis. The Mott–Schottky (M–S) plot and the C–V (capacitance per unit area *vs.* bias voltage) plot for four chosen solar cells are depicted in Fig. 13(a) and (b), respectively. The Mott–Schottky analysis, applied to C–V data, provides a means of evaluating the built-in voltage (V_{bi}) and charge carrier density

(N_d). The method is frequently employed in traditional p–n junction devices and semiconductor–metal contacts containing space-charge zones and constant depletion layers.[88] The value of the junction capacitance per unit area (C) is determined according to eqn (23):

$$\frac{1}{C^2} = \frac{2\varepsilon_0\varepsilon_r}{qN_d}(V_{bi} - V) \quad (23)$$

In eqn (23), ε_0 refers to the vacuum permittivity, ε_r indicates the dielectric constant of the donor material, q denotes the electronic charge, and V corresponds to the applied voltage (Fig. 13(b)).[101,102] The gradient of the straight portion is used to evaluate N_d, and V_{bi} is obtained by extending the fit to the voltage axis. As depicted in Fig. 13(a) and (b), the frequency stays constant at 1 MHz while the applied voltage sweeps between -0.8 V and 0.8 V. Among the four structures, the TiO$_2$ ETL-based device exhibited an exponential rise as voltage increased, while both LBSO and SnS$_2$ ETL-based devices displayed flat responses, and the ZnO ETL-based device showed a slight upward trend.

The M–S method, relying on capacitance–voltage relationships, has long been employed to assess space charge distribution in semiconductors arising from junction capacitance.[61] This method allows calculation of the built-in potential (V_{bi}) by examining the difference between electrode behavior and
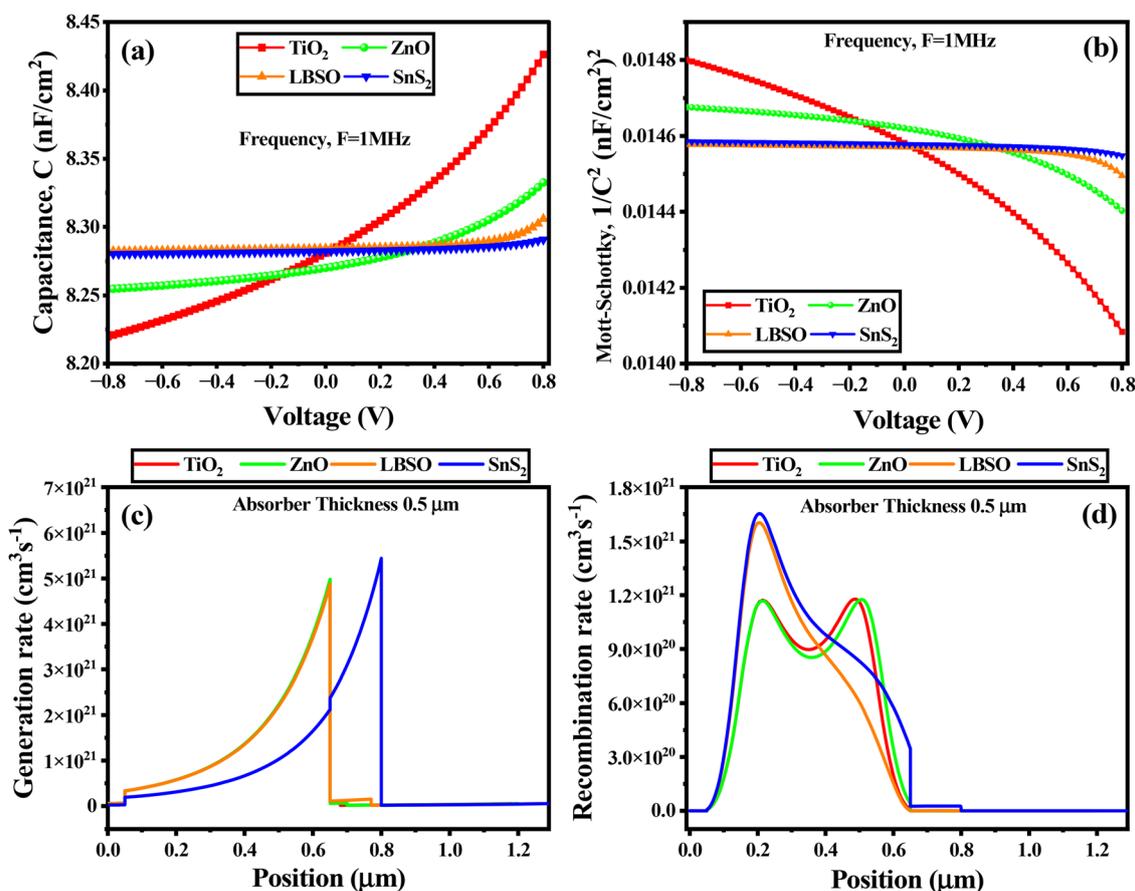

Fig. 13 Variations in (a) capacitance, (b) Mott–Schottky plot, and (c) generation and (d) recombination rates.

doping concentration.[103] In Fig. 13(b), the trend is the exact reverse of that shown in Fig. 13(a). In Fig. 13(b) where the TiO_2 ETL-based device decreases exponentially as voltage rises, LBSO and SnS_2 ETL devices remain almost constant, and the ZnO ETL-based device slightly declines.

2.8.11 Effect of generation and recombination rates. The generation rate represents the local creation of charge carriers within the device, dependent on the incident light's wavelength and the material's absorption characteristics. It indicates the quantity of electron–hole pairs produced at each location as a result of photon absorption at certain wavelengths. During carrier generation, an electron moves from the valence band to the conduction band, producing a hole and an electron–hole pair.[102] Generation and recombination rates for four different configurations are graphically depicted in Fig. 13(c) and (d). The generation of electron–hole pairs, $G(x)$, is determined using the incident photon flux, $N_{phot}(\lambda, x)$, along with SCAPS-1D as shown in eqn (24):

$$G(\lambda, x) = \alpha(\lambda, x) \times N_{phot}(\lambda, x) \qquad (24)$$

The generation rates peak at approximately 0.63 μm for TiO_2, ZnO, and LBSO ETL based configurations (Fig. 13(c)), while for the SnS_2 ETL based configuration the generation rate peaks at 0.8 μm.

The process of recombination involves electrons from the conduction band recombining with holes, thereby eliminating both carriers and acting as the opposite of generation.[104] The recombination rate in a solar cell depends on variables such as the density and lifetime of charge carriers.[61] Each configuration exhibits its highest recombination rate at about 0.2 μm. According to the figure, the SnS_2 ETL-based device demonstrates the greatest recombination rate among all configurations. The distribution of electron–hole recombination is affected by the formation of energy states within the solar cell. The recombination rate distribution experiences disruptions due to defects and grain boundaries.[57]

2.8.12 JV and QE characteristics. Current density represents the amount of electric current passing through a specific area and plays an important role in device evaluation.[88] Fig. 14(a) and (b) show the optimization process of the *J–V* characteristic curves and QE for the four different solar cell configurations. Fig. 14(a) shows that each structure displays a continuous process within the voltage range from 0.0 to 1.4 V, aligning with previous research.[63] Photocurrent decreases for each device in the voltage interval of about 1.4 to 1.6 V. Accurate
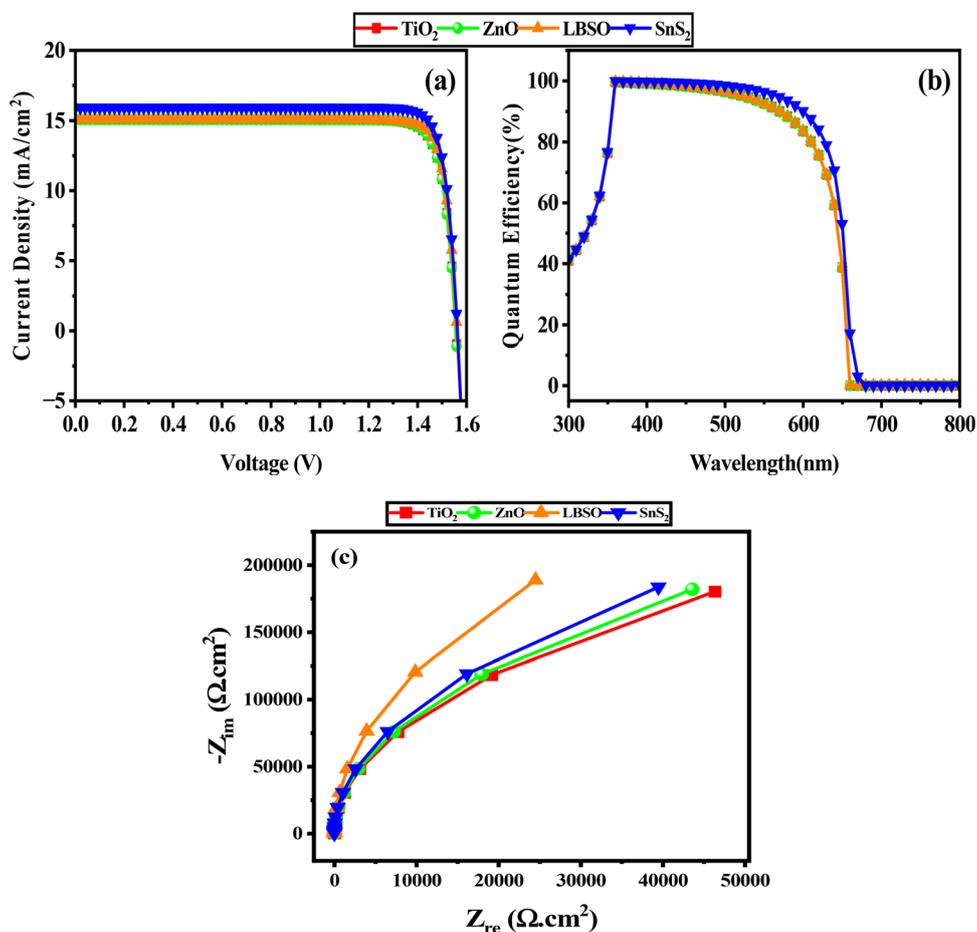

Fig. 14 (a) JV and (b) QE characteristics and (c) Nyquist plot.

assessment of photovoltaic parameters in a PSC requires insight into electron–hole recombination, which is depicted by the J–V curve of the perovskite layer. This corresponds to findings that improved perovskite crystallinity enhances performance by minimizing charge recombination.[35] The variation of quantum efficiency with the wavelength between 300 and 800 nm is presented in Fig. 14(b). At a wavelength of 350 nm, all PSCs achieved their highest QE, ranging from 98 to 99%, as depicted in the figure. Above 500 nm wavelength, all devices exhibit a reduction in quantum efficiency. The reduction in quantum efficiency at longer wavelengths is often attributed to free carrier absorption in heavily doped surface layers.[61] The findings indicate that higher voltage leads to improved quantum efficiency (QE) through diminished recombination. Enhancing the thickness of the absorber often results in higher quantum efficiency (QE), as it can absorb more photons.[105]

2.8.13 Nyquist plot. A Nyquist plot graphically represents the complex impedance of a system by plotting the imaginary part *versus* the real part, helping to analyze electrical characteristics like resistance and capacitance.[106,107] The impedance response of perovskite solar cells using diverse ETL materials is depicted in the Nyquist plot of Fig. 14(c). In this plot, the Y-axis corresponds to the geometric capacitance, highlighting the locations where carriers gather at the interface layers, while the X-axis denotes the recombination-related resistance. Each plot displays a single semicircle, corresponding to processes occurring in the frequency range of 1 Hz to 1 MHz. The Nyquist plot's semi-circle diameter for various ETL-based configurations highlights differences in electrical characteristics and performance outcomes. In the figure, it appears that each semi-circle begins at almost the same point. Approximately, the broad semi-circle observed in the Nyquist plot of the LBSO ETL-based structure suggests higher resistance, likely due to restricted charge transport or interfacial barriers. Conversely, the TiO$_2$ ETL-based device displays a noticeably smaller semi-circle, indicating lower resistance and more efficient charge transfer. The high-frequency resistance corresponds to the material's recombination resistance, while the associated capacitance at these

frequencies represents the geometric capacitance arising from charge accumulation at the interfaces.[108]

2.8.14 Comparison of SCAPS-1D findings to prior works. The expected photovoltaic outcomes for K$_2$NaInBr$_6$ PSCs are evaluated against the previous literature in Table 8. After final optimization, the cell performance efficiency of 20.44, 20.70, 21.9, and 20.42%, respectively, was observed for ETLs such as ZnO, LBSO, SnS$_2$, and TiO$_2$ with the Cu$_2$O HTL. The performance parameters of the K$_2$NaInBr$_6$-based solar cells are found to be comparable to or even exceed those of other lead-free perovskite alternatives, which have reported PCEs ranging from 1.66% to 16.23% (Table 8). Our study emphasizes the considerable potential of K$_2$NaInBr$_6$ as an alternative to conventional perovskites for achieving enhanced optoelectronic properties. Notably, K$_2$NaInBr$_6$ demonstrates marked improvements in V_{OC}, J_{SC}, and FF relative to other lead-free perovskites (Table 8). These enhancements underline its promise for future applications in high-performance solar cells. Compared to ZnO and TiO$_2$ ETL-based devices, which demonstrate almost similar PSC performance parameters, the ITO/SnS$_2$/K$_2$NaInBr$_6$/Cu$_2$O/Ni PSC achieves the highest performance, with performance parameters V_{OC} of 1.5637 V, J_{SC} of 15.9286 mA cm^{-2}, FF of 87.75%, and PCE of 21.9%. The observed difference arises primarily from the superior J_{SC} of our devices, which results from optimal ETL and HTL choices. The integration of SCAPS-1D simulations and DFT calculations in our design provides an innovative framework for enhancing solar cell performance in future applications. The observed enhancement in performance suggests strong prospects for K$_2$NaInBr$_6$ in photovoltaic technologies. The results underscore that selecting suitable ETL and HTL materials is key to maximizing solar cell efficiency.

3. Limitations and guidelines for experimental validation

This study highlights the optoelectronic potential of K$_2$NaInBr$_6$-based solar cells with Cu$_2$O as the HTL and various ETLs

Table 8 Experimental and theoretical comparison of PV parameters

No.	Optimized devices	Types^a	V_{OC} (V)	J_{SC} (mA cm^{-2})	FF (%)	PCE (%)	Ref.
1	FTO/SnO$_2$/Cs$_2$CuBiCl$_6$/Cu$_2$O/Au	E	0.98	4.05		1.87	109
2	FTO/TiO$_2$/Cs$_2$AgBiBr$_6$/spiro-OMeTAD/Au	E	1.057	3.87	40.58	1.66	110
3	Glass/FTO/TiO$_2$/Cs$_2$AgBiBr$_6$/Cu$_2$O/Au	T	1.5	11.45	42.1	7.25	111
4	FTO/TiO$_2$/Cs$_2$AgSbBr$_6$/spiro-OMeTAD/Ag	T	0.94	22.49	50.2	10.70	112
5	FTO/Ws$_2$/Cs$_2$CuBiBr$_6$/spiro-OMeTAD/Ag	T	0.60	34.59	67.36	14.08	112
6	FTO/TiO$_2$/Cs$_2$AgBiBr$_6$/spiro-OMeTAD/MoO$_3$/Ag	E	1.01	3.82	65	2.51	113
7	FTO/TiO$_2$/Cs$_2$AgBiBr$_6$/spiro-OMeTAD/Au	E	0.98	3.96	62.40	2.43	114
8	ITO/TiO$_2$/Cs$_2$Ag BiCl$_6$/Cu$_2$O/Au	T	0.96	10.04	84.48	8.21	115
9	ITO/BaSnO$_3$/K$_2$CuBiBr$_6$/NiO/Au	T	0.98	29.20	55.88	14.70	116
10	Ohmic contact/spiro-OMeTAD/Cs$_2$BiAgI$_6$/ TiO$_2$/SnO$_2$:F(ZnO$_2$)/ohmic contact	T	1.18	16.2	80.20	15.90	117
11	FTO/PCBM/Cs$_2$BiAgI$_6$/PTAA	T	1.08	19.94	74.87	16.23	117
12	ITO/ZnO/K$_2$NaInBr$_6$/Cu$_2$O/Ni	T	1.5565	15.094318	86.99	20.44	This work
13	ITO/LBSO/K$_2$NaInBr$_6$/Cu$_2$O/Ni	T	1.5620	15.094806	87.80	20.70	This work
14	ITO/SnS$_2$/K$_2$NaInBr$_6$/Cu$_2$O/Ni	T	1.5637	15.928609	87.75	21.9	This work
15	ITO/TiO$_2$/K$_2$NaInBr$_6$/Cu$_2$O/Ni	T	1.5569	15.094243	86.88	20.42	This work

^{a} Note: T = theoretical, E = experimental.

(ZnO, LBSO, SnS$_2$ and TiO$_2$); yet simulation-based analysis has inherent limitations. Computational models cannot fully replicate real-world device behavior, particularly regarding long-term stability, thermal tolerance, interfacial degradation, and environmental impacts. Fabricating multilayer devices with precise interfaces, especially using novel ETLs and inorganic absorbers, adds further complexity, often creating gaps between simulated and experimental efficiencies. Future work should focus on experimental validation, assessing stability, reproducibility, and performance under diverse illumination, temperature, and humidity conditions. Compatibility with scalable deposition methods such as sputtering, spin-coating, or vapor-phase processing must also be evaluated. A systematic experimental framework from material synthesis to stability testing will be essential to confirm the practical feasibility and photovoltaic performance of K$_2$NaInBr$_6$, ultimately validating the predictions of this study.

4. Conclusion

This investigation combines first-principles and SCAPS-1D simulations to analyze K$_2$NaInBr$_6$, showcasing its advantageous structural, electronic, and optical features for solar energy conversion. Structural stability is ensured by tolerance factor determination and the presence of negative formation and binding energies. Electronic analysis using PBE and PBEsol functionals confirms that the material exhibits a direct band gap and semiconducting behavior. The computed direct band gaps, using PBE and PBEsol, align with the optimal range for photovoltaics, ensuring enhanced light absorption and charge carrier production. The analysis of TDOS and PDOS provides insights into bonding characteristics and orbital hybridization. The optical study reveals strong absorption coefficients ($\sim 10^5$ cm^{-1}), coupled with favorable features including low energy loss and reduced reflectivity, particularly across the visible to UV region. Device simulations were carried out using the K$_2$NaInBr$_6$ double halide perovskite absorber in solar cell architectures incorporating four different ETL and six HTL materials. Among the explored architectures, the ITO/SnS$_2$/K$_2$NaInBr$_6$/CuO$_2$/Ni device exhibited the highest efficiency, resulting from favorable band structure alignment, efficient charge extraction, and reduced recombination losses. The peak photovoltaic efficiency theoretically under idealized assumptions (SCAPS-1D parameterization) was recorded 21.9% for this device at a 600 nm optimized thickness and is not anticipated to be experimentally achievable without optimized improvements in materials and interfaces. The results indicate that defect density (N_t, from 1×10^{13} to 1×10^{17} cm^{-3}) and absorber thickness (0.3–0.7 μm) have a significant impact on device performance. The effects of the left metal contact were also investigated. R_s predominantly influenced the FF and PCE, while V_{OC} and J_{SC} remained largely unaffected. Conversely, an increase in R_{sh} led to improvements in V_{OC}, J_{SC}, FF, and PCE, with the best performance observed at 10^3 Ω cm^2. Temperature variations from 270 to 470 K negatively affected V_{OC}, FF, and

PCE, although J_{SC} remained stable. The study also examined capacitance properties, Mott–Schottky behavior, QE, and J–V characteristics, along with charge generation and recombination dynamics. Nyquist plot analysis revealed differences in charge transfer and impedance behavior. Additionally, the cubic crystal structure of K$_2$NaInBr$_6$ was confirmed through evaluation of the Goldschmidt tolerance factor, the octahedral factor, and a recently proposed tolerance parameter. This research lays the groundwork for subsequent experimental and computational studies, advancing environmentally sustainable and high-performance lead-free solar devices.

Author contributions

Nazmul Shahadath: investigation, methodology, data curation, conceptualization, writing original manuscript; Ashraful Mujahid: investigation, methodology, data curation, review – editing; Raihan Kabir: formal analysis, software, methodology, review – editing; Md. Tarekuzzaman: formal analysis, software, conceptualization, review – editing; Mohammad Yasin Hayat Khan: formal analysis, software, conceptualization, review – editing; Md. Abu Bakkar Siddique: formal analysis, data curation, review – editing; Sohail Ahmad: formal analysis, data curation, review – editing; Md. Rasheduzzaman: formal analysis, validation, review – editing; Md. Zahid Hasan: formal analysis, validation, supervision, review – editing.

Conflicts of interest

There is no conflict to declare.

Data availability

Additional raw data or calculation files are available from the corresponding author upon reasonable request.

Supplementary information (SI): the computational input files, output data, and SCAPS simulation files. See DOI: https://doi.org/10.1039/d6ma00042h.

Acknowledgements

References

1 P. Metrangolo, L. Canil, A. Abate, G. Terraneo and G. Cavallo, Halogen Bonding in Perovskite Solar Cells: A New Tool for Improving Solar Energy Conversion, *Angew. Chem., Int. Ed.*, 2022, **61**(11), e202114793, DOI: 10.1002/anie.202114793.

2 B. Xin, N. Alaal, S. Mitra, A. Subahi, Y. Pak, D. Almalawi, N. Alwadai, S. Lopatin and I. S. Roqan, Identifying Carrier Behavior in Ultrathin Indirect-Bandgap CsPbX3 Nanocrystal

Films for Use in UV/Visible-Blind High-Energy Detectors, *Small*, 2020, **16**(43), 2004513, DOI: 10.1002/smll.202004513.

3 Targeting high performance of perovskite solar cells by combining electronic, manufacturing and environmental features in machine learning techniques: Heliyon. https://www.cell.com/heliyon/fulltext/S2405-8440(23)08706-6 (accessed 2025-08-12).

4 P. Gao, M. Grätzel and M. K. Nazeeruddin, Organohalide Lead Perovskites for Photovoltaic Applications, *Energy Environ. Sci.*, 2014, **7**(8), 2448–2463, DOI: 10.1039/C4EE00942H.

5 G. Ho Gu, J. Noh, I. Kim and Y. Jung, Machine Learning for Renewable Energy Materials, *J. Mater. Chem. A*, 2019, **7**(29), 17096–17117, DOI: 10.1039/C9TA02356A.

6 A. Di Nardo, M. Calabrese, V. Venezia, M. Portarapillo, M. Turco, A. Di Benedetto and G. Luciani, Addressing Environmental Challenges: The Role of Hydrogen Technologies in a Sustainable Future, *Energies*, 2023, **16**(23), 7908, DOI: 10.3390/en16237908.

7 M. Woźniak, A. Badora, K. Kud and L. Woźniak, Renewable Energy Sources as the Future of the Energy Sector and Climate in Poland—Truth or Myth in the Opinion of the Society, *Energies*, 2022, **15**(1), 45, DOI: 10.3390/en15010045.

8 B. L. Smith, M. Woodhouse, K. A. W. Horowitz, T. J. Silverman, J. Zuboy and R. M. Margolis, *Photovoltaic (PV) Module Technologies: 2020 Benchmark Costs and Technology Evolution Framework Results*, NREL/TP-7A40-78173; National Renewable Energy Laboratory (NREL), Golden, CO (United States), 2021, DOI: 10.2172/1829459.

9 M. K. Hossain, G. A. Raihan, M. A. Akbar, M. H. Kabir Rubel, M. H. Ahmed, Md. I. Khan, S. Hossain, S. K. Sen, M. I. E. Jalal and A. El-Denglawey, Current Applications and Future Potential of Rare Earth Oxides in Sustainable Nuclear, Radiation, and Energy Devices: A Review, *ACS Appl. Electron. Mater.*, 2022, **4**(7), 3327–3353, DOI: 10.1021/acsaelm.2c00069.

10 S. K. Pranta, R. B. Khan, A. S. Tanjeem, A. Mujahid, R. Chowdhury and A. Shufian, Techno-Economic Study of Solar-Hydrogen Hybrid Charging Infrastructure for Electric Vehicles in Bangladesh. In202 2025 Jul 31 (pp. 1-6). IEEE., *2025 International Conference on Quantum Photonics, Artificial Intelligence, and Networking (QPAIN)*, 2026, 1–6, DOI: 10.1109/QPAIN66474.2025.11171934.

11 M. S. Rahman, R. B. Khan, A. Mujahid, A. H. Mahedi, M. S. Sajib and R. Chowdhury, Design and Feasibility Analysis of a 1MWp Grid-Connected Floating Solar Photovoltaic Plant in Kaptai, Bangladesh, *2024 International Conference on Innovations in Science, Engineering and Technology (ICISET)*, 2024 Oct 26, 1–6, DOI: 10.1109/ICISET62123.2024.10939890.

12 Lewis and S. Nathan, Research opportunities to advance solar energy utilization, *Science*, 2016, **351**(6271), aad1920, DOI: 10.1126/science.aad1920.

13 M. A. Green and A. Ho-Baillie, Perovskite Solar Cells: The Birth of a New Era in Photovoltaics, *ACS Energy Lett.*, 2017, **2**(4), 822–830, DOI: 10.1021/acsenergylett.7b00137.

14 A. Kojima, K. Teshima, Y. Shirai and T. Miyasaka, Organometal Halide Perovskites as Visible-Light Sensitizers for Photovoltaic Cells, *J. Am. Chem. Soc.*, 2009, **131**(17), 6050–6051, DOI: 10.1021/ja809598r.

15 H.-S. Kim, C.-R. Lee, J.-H. Im, K.-B. Lee, T. Moehl, A. Marchioro, S.-J. Moon, R. Humphry-Baker, J.-H. Yum, J. E. Moser, M. Grätzel and N.-G. Park, Lead Iodide Perovskite Sensitized All-Solid-State Submicron Thin Film Mesoscopic Solar Cell with Efficiency Exceeding 9%, *Sci. Rep.*, 2012, **2**(1), 591, DOI: 10.1038/srep00591.

16 W. S. Yang, B.-W. Park, E. H. Jung, N. J. Jeon, Y. C. Kim, D. U. Lee, S. S. Shin, J. Seo, E. K. Kim, J. H. Noh and S. I. Seok, Iodide Management in Formamidinium-Lead–Halide–Based Perovskite Layers for Efficient Solar Cells, *Science*, 2017, **356**(6345), 1376–1379, DOI: 10.1126/science.aan2301.

17 N. J. Jeon, H. Na, E. H. Jung, T.-Y. Yang, Y. G. Lee, G. Kim, H.-W. Shin, S. Il Seok, J. Lee and J. Seo, A Fluorene-Terminated Hole-Transporting Material for Highly Efficient and Stable Perovskite Solar Cells, *Nat. Energy*, 2018, **3**(8), 682–689, DOI: 10.1038/s41560-018-0200-6.

18 D. Abdullah and D. C. Gupta, Exploring the Structural, Mechanical, Electronic, Optical, and Thermoelectric Properties of Cesium-Based Double Perovskite Cs_2GeSnX_6 (X = Cl, Br, I) Compounds: A DFT Study, *Mater. Sci. Semicond. Process.*, 2023, **167**, 107813, DOI: 10.1016/j.mssp.2023.107813.

19 M. A. Ali, A. A. Alothman, M. Mushab and M. Faizan, Electronic, Optical and Thermoelectric Properties of Stable A_2LiIO_6 (A = Sr, Ba) Lead-Free Double Perovskites for Low-Cost Energy Applications, *J. Inorg. Organomet. Polym.*, 2024, **34**(7), 3270–3280, DOI: 10.1007/s10904-024-03109-0.

20 S. Bimli, V. Manjunath, S. R. Mulani, A. Miglani, O. S. Game and R. S. Devan, Theoretical Investigations of All Inorganic Cs_2SnI_6 Double Perovskite Solar Cells for Efficiency ∼30%, *Sol. Energy*, 2023, **256**, 76–87, DOI: 10.1016/j.solener.2023.03.059.

21 M. S. Uddin, M. K. Hossain, M. B. Uddin, G. F. I. Toki, M. Ouladsmane, M. H. K. Rubel, D. I. Tishkevich, P. Sasikumar, R. Haldhar and R. Pandey, An In-Depth Investigation of the Combined Optoelectronic and Photovoltaic Properties of Lead-Free $Cs_2AgBiBr_6$ Double Perovskite Solar Cells Using DFT and SCAPS-1D Frameworks, *Adv. Electron. Mater.*, 2024, **10**(5), 2300751, DOI: 10.1002/aelm.202300751.

22 A. Kumar, A. Kumar and V. Krishnan, Perovskite Oxide Based Materials for Energy and Environment-Oriented Photocatalysis, *ACS Catal.*, 2020, **10**(17), 10253–10315, DOI: 10.1021/acscatal.0c02947.

23 M. K. Hossain, A. A. Arnab, D. P. Samajdar, M. H. K. Rubel, M. M. Hossain, Md. R. Islam, R. C. Das, H. Bencherif, Md. F. Rahman, J. Madan, R. Pandey, S. Bhattarai, M. Amami and D. K. Dwivedi, Design Insights into La_2NiMnO_6-Based Perovskite Solar Cells Employing Different Charge Transport Layers: DFT and SCAPS-1D Frameworks, *Energy Fuels*, 2023, **37**(17), 13377–13396, DOI: 10.1021/acs.energyfuels.3c02361.

24 T. Sangavi, S. Vasanth, C. Viswanathan and N. Ponpandian, Synergizing Experimental and Theoretical Insights: Unveiling the Solar Potential of La_2NiMnO_6 Double Perovskite for

Enhanced Efficiency and Sustainability in Photovoltaics, *Chem. Eng. J.*, 2024, **486**, 150216, DOI: 10.1016/j.cej.2024.150216.

25 Experimental and Theoretical Investigation of the Structural and Opto-electronic Properties of Fe-Doped Lead-Free $Cs_2AgBiCl_6$ Double Perovskite, *Chem. – Eur. J.*, 2021Wiley Online Library. https://chemistry-europe.onlinelibrary.wiley.com/doi/full/10.1002/chem.202004902 (accessed 2025-07-30).

26 K. Assiouan, A. Marjaoui, J. E. L. Khamkhami, M. Zanouni, H. Ziani, A. Bouchrit and A. Achahbar, Theoretical Investigation of Rb_2AuBiX_6 (X = Br, Cl, F) Double Perovskite for Thermoelectric and Optoelectronic Applications, *J. Phys. Chem. Solids*, 2024, **188**, 111890, DOI: 10.1016/j.jpcs.2024.111890.

27 S. A. Shah, M. Husain, V. Tirth, A. Azzouz-Rached, N. Rahman and A. Khan, First-Principles Calculations to Investigate the Structural, Electronic, Optical, Mechanical, and Thermodynamic Properties of Double Perovskites $Ba_2WB'O_6$ (B' = Co, Fe, Mn, Ni, and Zn), *Optik*, 2024, **300**, 171636, DOI: 10.1016/j.ijleo.2024.171636.

28 G. Ayub, N. Rahman, M. Husain, M. Sohail, R. Khan, N. Sfina, M. Elhadi, A. Azzouz-Rached and A. Alotaibi, Tailoring the Structural, Elastic, Electronic, and Optical Properties of Cs_2ScCuX_6 (X = Cl and F) Double Perovskite Compounds via Density Functional Theory (DFT, *J. Phys. Chem. Solids*, 2024, **188**, 111942, DOI: 10.1016/j.jpcs.2024.111942.

29 G. Ayub, M. Husain, N. Sfina, R. Khan, M. Sohail, H. S. Waheed, M. Elhadi, B. S. Abdullaeva and N. Rahman, Exploring the Properties of Quaternary X_2NaTlF_6 (X = Cs, Rb) Halide Double Perovskite Materials for Energy Conversion, Harvesting, and Storage Using Density Functional Theory, *Opt. Quantum Electron.*, 2023, **56**(1), 11, DOI: 10.1007/s11082-023-05669-w.

30 I. Alam, R. Mollick and M. A. Ashraf, Numerical Simulation of $Cs_2AgBiBr_6$-Based Perovskite Solar Cell with ZnO Nanorod and P3HT as the Charge Transport Layers, *Phys. B*, 2021, **618**, 413187, DOI: 10.1016/j.physb.2021.413187.

31 J. Gong, S. B. Darling and F. You, Perovskite Photovoltaics: Life-Cycle Assessment of Energy and Environmental Impacts, *Energy Environ. Sci.*, 2015, **8**(7), 1953–1968, DOI: 10.1039/C5EE00615E.

32 D. Jayan K, V. Sebastian and J. Kurian, Simulation and Optimization Studies on $CsPbI_3$ Based Inorganic Perovskite Solar Cells, *Sol. Energy*, 2021, **221**, 99–108, DOI: 10.1016/j.solener.2021.04.030.

33 H. Bencherif, L. Dehimi, N. Mahsar, E. Kouriche and F. Pezzimenti, Modeling and Optimization of CZTS Kesterite Solar Cells Using TiO_2 as Efficient Electron Transport Layer, *Mater. Sci. Eng., B*, 2022, **276**, 115574, DOI: 10.1016/j.mseb.2021.115574.

34 F. Kherrat, L. Dehimi, H. Bencherif, M. M. A. Moon, M. K. Hossain, N. A. Sonmez, T. Ataser, Z. Messai and S. Özçelik, Performance Enhancement of Eco-Friendly $Cs_3Sb_2I_9$-Based Perovskite Solar Cell Employing Nb_2O_5 and CuI as Efficient

Charge Transport Layers, *Micro Nanostruct.*, 2023, **183**, 207676, DOI: 10.1016/j.micrna.2023.207676.

35 M. Liu, M. B. Johnston and H. J. Snaith, Efficient Planar Heterojunction Perovskite Solar Cells by Vapour Deposition, *Nature*, 2013, **501**(7467), 395–398, DOI: 10.1038/nature12509.

36 M. A. Madanat, A. A. Al-Tabbakh, M. Alsa'eed, H. Al-Dmour and M. S. Mousa, Application of Murphy – Good Plot Parameters Extraction Method on Electron Emission from Carbon Fibers, *Ultramicroscopy*, 2022, **234**, 113479, DOI: 10.1016/j.ultramic.2022.113479.

37 R. T. Ako, P. Ekanayake, D. J. Young, J. Hobley, V. Chellappan, A. L. Tan, S. Gorelik, G. S. Subramanian and C. M. Lim, Evaluation of Surface Energy State Distribution and Bulk Defect Concentration in DSSC Photoanodes Based on Sn, Fe, and Cu Doped TiO2, *Appl. Surf. Sci.*, 2015, **351**, 950–961, DOI: 10.1016/j.apsusc.2015.06.015.

38 S. Z. Haider, H. Anwar and M. Wang, A Comprehensive Device Modelling of Perovskite Solar Cell with Inorganic Copper Iodide as Hole Transport Material, *Semicond. Sci. Technol.*, 2018, **33**(3), 035001, DOI: 10.1088/1361-6641/aaa596.

39 Z. Zhang, Q. Sun, Y. Lu, F. Lu, X. Mu, S.-H. Wei and M. Sui, Hydrogenated $Cs_2AgBiBr_6$ for Significantly Improved Efficiency of Lead-Free Inorganic Double Perovskite Solar Cell, *Nat. Commun.*, 2022, **13**(1), 3397, DOI: 10.1038/s41467-022-31016-w.

40 M. H. K. Rubel, M. A. Hossain, M. K. Hossain, K. M. Hossain, A. A. Khatun, M. M. Rahaman, Md Ferdous Rahman, M. M. Hossain and J. Hossain, First-Principles Calculations to Investigate Structural, Elastic, Electronic, Thermodynamic, and Thermoelectric Properties of $CaPd_3B_4O_{12}$ (B = Ti, V) Perovskites, *Results Phys.*, 2022, **42**, 105977, DOI: 10.1016/j.rinp.2022.105977.

41 M. I. Kholil, M. T. H. Bhuiyan, M. A. Rahman, M. S. Ali and M. Aftabuzzaman, Effects of Fe Doping on the Visible Light Absorption and Bandgap Tuning of Lead-Free (CsSnCl3) and Lead Halide (CsPbCl3) Perovskites for Optoelectronic Applications, *AIP Adv.*, 2021, **11**(3), 035229, DOI: 10.1063/5.0042847.

42 A. M. Alanazi, H. Al Dmour, S. A. Popoola, H. Oudghiri Hassani, S. Rakass, R. Al-Faze and F. Kooli, Parameters Synthesis of Na-Magadiite Materials for Water Treatment and Removal of Basic Blue-41: Properties and Single-Batch Design Adsorber, *Inorganics*, 2023, **11**(11), 423, DOI: 10.3390/inorganics11110423.

43 N. Y. Dzade, First-Principles Insights into the Electronic Structure, Optical and Band Alignment Properties of Earth-Abundant Cu_2SrSnS_4 Solar Absorber, *Sci. Rep.*, 2021, **11**(1), 4755, DOI: 10.1038/s41598-021-84037-8.

44 A. Jain, Y. Shin and K. A. Persson, Computational Predictions of Energy Materials Using Density Functional Theory, *Nat. Rev. Mater.*, 2016, **1**(1), 15004, DOI: 10.1038/natrevmats.2015.4.

45 M. S. Yagoub and M. Adnane, Simulation Of PEDOT: PSS Solid-State CdS Quantum Dot Solar Cells With TiO2 Ultrathin

Film Via SCAPS-1D, *J. Opt.*, 2024, 1–2, DOI: 10.1007/s12596-024-02267-1.

46 S. H. Godasiaei, Optimizing the Performance of Vapor-Deposited Perovskite Solar Cells through Advanced Predictive Modeling, *J. Mater. Sci.*, 2024, **59**(21), 9398–9422, DOI: 10.1007/s10853-024-09802-2.

47 L. Song, Perovskite Solar Cells toward Industrialization: Screen Printed Perovskite Films, *Mater. Rep.: Energy*, 2022, **2**(4), 100171, DOI: 10.1016/j.matre.2022.100171.

48 J. Wu, M. Gao, Y. Chai, P. Liu, B. Zhang, J. Liu and L. Ye, Towards a Bright Future: The Versatile Applications of Organic Solar Cells, *Mater. Rep.: Energy*, 2021, **1**(4), 100062, DOI: 10.1016/j.matre.2021.100062.

49 A. B. Siad, H. Riane, M. B. Siad, F. Z. Dahou, A. Allouche and M. Baira, Elevating Energy Device Potential: Exploring Optoelectronic and Thermoelectric Advantages in Stable Double Perovskites K_2NaInX_6 (X = F, Cl, Br, I) via Ab Initio Analysis, *J. Mater. Sci.*, 2024, **59**(5), 1989–2007, DOI: 10.1007/s10853-023-09229-1.

50 K. Schwarz, DFT Calculations of Solids with LAPW and WIEN2k, *J. Solid State Chem.*, 2003, **176**(2), 319–328, DOI: 10.1016/S0022-4596(03)00213-5.

51 J. P. Perdew, K. Burke and M. Ernzerhof, Generalized Gradient Approximation Made Simple, *Phys. Rev. Lett.*, 1996, **77**(18), 3865–3868, DOI: 10.1103/PhysRevLett.77.3865.

52 J. P. Perdew, A. Ruzsinszky, G. I. Csonka, O. A. Vydrov, G. E. Scuseria, L. A. Constantin, X. Zhou and K. Burke, Restoring the Density-Gradient Expansion for Exchange in Solids and Surfaces, *Phys. Rev. Lett.*, 2008, **100**(13), 136406, DOI: 10.1103/PhysRevLett.100.136406.

53 M. A. Hadi, R. V. Vovk and A. Chroneos, Physical Properties of the Recently Discovered $Zr2(Al_{1-x}Bi_x)C$ MAX Phases, *J. Mater. Sci.: Mater. Electron.*, 2016, **27**(11), 11925–11933, DOI: 10.1007/s10854-016-5338-z.

54 Md. M. Hossain, Md. A. Ali, Md. M. Uddin, S. H. Naqib and A. K. M. A. Islam, Newly Synthesized Three-Dimensional Boron-Rich Chalcogenides B12X (X = S and Se): Theoretical Characterization of the Physical Properties for Optoelectronic and Mechanical Applications, *ACS Omega*, 2021, **6**(49), 33899–33913, DOI: 10.1021/acsomega.1c05172.

55 R. A. Jabr, M. Hamad and Y. Mohanna, Newton-Raphson Solution of Poisson's Equation in a Pn Diode, *Int. J. Electr. Eng. Educ.*, 2007, **44**, 23–33, DOI: 10.7227/IJEEE.44.1.3.

56 S. Bhattarai and T. D. Das, Optimization of Carrier Transport Materials for the Performance Enhancement of the MAGeI3 Based Perovskite Solar Cell, *Sol. Energy*, 2021, **217**, 200–207, DOI: 10.1016/j.solener.2021.02.002.

57 M. K. Hossain, M. H. K. Rubel, G. F. I. Toki, I. Alam, Md. F. Rahman and H. Bencherif, Effect of Various Electron and Hole Transport Layers on the Performance of CsPbI3-Based Perovskite Solar Cells: A Numerical Investigation in DFT, SCAPS-1D, and wxAMPS Frameworks, *ACS Omega*, 2022, **7**(47), 43210–43230, DOI: 10.1021/acsomega.2c05912.

58 A. Mujahid, M. Y. Hayat Khan, M. Mayen Uddin, F. A. Alamer, O. Alsalmi, M. Rasheduzzaman and M. Zahid Hasan, Computational Modeling and Photovoltaic Performance Evaluation of Various ETL/HTL Engineered CsCdI3-Based Perovskite Solar Cell Architectures, *RSC Adv.*, 2025, **15**(39), 32679–32707, DOI: 10.1039/D5RA05441A.

59 A. Mujahid, M. H. Mia, O. Alsalmi and M. Z. Hasan, Integrated simulation of $Li_2AgBiBr_6$ solar harvesters: Device-level engineering and module-level forecasting, *J. Power Sources*, 2026, **671**, 239573, DOI: 10.1016/j.jpowsour.2026.239573.

60 M. K. Hossain, O. Alsalman, S. Rana, M. S. Uddin, G. F. I. Toki, S. H. Shahatha, M. R. Mohammad, M. A. Darwish, P. Sasikumar, S. Haq, H. Bencherif and R. Haldhar, Enhancing Efficiency and Performance of Cs_2TiI_6-Based Perovskite Solar Cells through Extensive Optimization: A Numerical Approach, *Inorg. Chem. Commun.*, 2024, **168**, 112964, DOI: 10.1016/j.inoche.2024.112964.

61 M. K. Hossain, M. K. A. Mohammed, R. Pandey, A. A. Arnab, M. H. K. Rubel, K. M. Hossain, M. H. Ali, Md. F. Rahman, H. Bencherif, J. Madan, Md. R. Islam, D. P. Samajdar and S. Bhattarai, Numerical Analysis in DFT and SCAPS-1D on the Influence of Different Charge Transport Layers of $CsPbBr_3$ Perovskite Solar Cells, *Energy Fuels*, 2023, **37**(8), 6078–6098, DOI: 10.1021/acs.energyfuels.3c00035.

62 M. K. Hossain, G. F. I. Toki, A. Kuddus, M. H. K. Rubel, M. M. Hossain, H. Bencherif, Md. F. Rahman, Md. R. Islam and M. Mushtaq, An Extensive Study on Multiple ETL and HTL Layers to Design and Simulation of High-Performance Lead-Free CsSnCl3-Based Perovskite Solar Cells, *Sci. Rep.*, 2023, **13**(1), 2521, DOI: 10.1038/s41598-023-28506-2.

63 M. A. Bakkar Siddique, M. S. Parves, M. Tarekuzzaman, M. R. Kabir, M. S. M. Al-Saleem, J. Y. Al-Humaidi, M. Rasheduzzaman, M. M. Hossen, M. M. Rahman and M. Z. Hasan, Exploring Optoelectronic Behavior and Solar Cell Efficiency of Double Halide Perovskites M_2KIrCl_6 (M = Cs, Rb) through DFT and SCAPS-1D, *Langmuir*, 2025, **41**(30), 19797–19820, DOI: 10.1021/acs.langmuir.5c01639.

64 Md Atikur Rahman, W. Hasan, R. Khatun, Md Zahid Hasan, Md Hafijur Rahman, S. Sarker, M. Hasan and J. F. Lubna, An Ab-Initio Study to Investigate the Structural, Mechanical, Electrical, Optical and Thermal Properties of the AZrO3 (A= Mg, Ca, Sr, Ba, Sn, Cu) Compounds, *Mater. Today Commun.*, 2023, **34**, 105339, DOI: 10.1016/j.mtcomm.2023.105339.

65 X. Du, D. He, H. Mei, Y. Zhong and N. Cheng, Insights on Electronic Structures, Elastic Features and Optical Properties of Mixed-Valence Double Perovskites $Cs_2Au_2X_6$ (X = F, Cl, Br, I), *Phys. Lett. A*, 2020, **384**(8), 126169, DOI: 10.1016/j.physleta.2019.126169.

66 S. Mahmud, M. A. Ali, M. M. Hossain and M. M. Uddin, DFT Aided Prediction of Phase Stability, Optoelectronic and Thermoelectric Properties of A_2AuScX_6 (A= Cs, Rb; X= Cl, Br, I) Double Perovskites for Energy Harvesting Technology, *Vacuum*, 2024, **221**, 112926, DOI: 10.1016/j.vacuum.2023.112926.

67 Y. Liang, Exploring Inorganic and Nontoxic Double Perovskites $Cs_2AgInBr_{6(1-x)}Cl_{6x}$ from Material Selection to Device Design in Material Genome Approach, *J. Alloys*

Compd., 2021, **862**, 158575, DOI: 10.1016/j.jallcom.2020. 158575.

68 A. Dasgupta, S. Sen, P. Singh and A. Raman, A Comprehensive Overview of the Foundations of Semiconductor Materials, *Semiconductor Nanoscale Devices: Materials and Design Challenges*, Bentham Science Publishers, 2025, pp. 80–109.

69 M. D. Tarekuzzaman, M. H. Ishraq, M. D. A. Rahman, A. Irfan, M. D. Z. Rahman, M. S. Akter, S. Abedin, M. A. Rayhan, M. D. Rasheduzzaman, M. M. Hossen and M. D. Z. Hasan, A Systematic First-Principles Investigation of the Structural, Electronic, Mechanical, Optical, and Thermodynamic Properties of Half-Heusler ANiX (A = Sc, Ti, Y, Zr, Hf; X = Bi, Sn) for Spintronics and Optoelectronics Applications, *J. Comput. Chem.*, 2024, **45**(29), 2476–2500, DOI: 10.1002/jcc.27455.

70 M. Tarekuzzaman, N. Shahadath, M. Montasir, O. Alsalmi, H. Mia, M. Al-Dmour, H. Rasheduzzaman and M. Zahid Hasan, DFT Analysis of the Physical Properties of Direct Band Gap Semiconducting Double Perovskites A 2 BIrCl 6 (A = Cs, Rb; B = Na, K) for Solar Cells and Optoelectronic Applications, *RSC Adv.*, 2025, **15**(17), 13643–13661, DOI: 10.1039/D5RA01748C.

71 B. K. Ravidas, M. K. Roy and D. P. Samajdar, Design Insights and Photovoltaic Performance Analysis of Non-Lead Inorganic RbSnX3 (X = I, Br, Cl) Perovskites through Coupled Density Functional Theory and SCAPS-1D Simulation Frameworks, *ACS Appl. Electron. Mater.*, 2024, **6**(7), 5126–5150, DOI: 10.1021/acsaelm.4c00670.

72 D. Behera, R. Sharma, H. Ullah, H. S. Waheed and S. K. Mukherjee, Electronic, Optical, and Thermoelectric Investigations of Zintl Phase AAg$_2$Se$_2$ (A = Sr, Ba) Compounds: A First-Principle Approach, *J. Solid State Chem.*, 2022, **312**, 123259, DOI: 10.1016/j.jssc.2022.123259.

73 R. Gaillac, P. Pullumbi and F.-X. Coudert, ELATE: An Open-Source Online Application for Analysis and Visualization of Elastic Tensors, *J. Phys.: Condens. Matter*, 2016, **28**(27), 275201, DOI: 10.1088/0953-8984/28/27/275201.

74 Y. Liu, I. J. Cleveland, M. N. Tran and E. S. Aydil, Stability of the Halide Double Perovskite Cs$_2$AgInBr$_6$, *J. Phys. Chem. Lett.*, 2023, **14**(12), 3000–3006, DOI: 10.1021/acs.jpclett. 3c00303.

75 H. Chorsi, B. Cheng, B. Zhao, J. Toudert, V. Asadchy, O. F. Shoron, S. Fan and R. Matsunaga, Topological Materials for Functional Optoelectronic Devices, *Adv. Funct. Mater.*, 2022, **32**(19), 2110655, DOI: 10.1002/adfm.202110655.

76 W. Wang and L. Qi, Light Management with Patterned Micro-and Nanostructure Arrays for Photocatalysis, Photovoltaics, and Optoelectronic and Optical Devices, *Adv. Funct. Mater.*, 2019, **29**(25), 1807275, DOI: 10.1002/adfm.201807275.

77 M. Manzoor, D. Bahera, R. Sharma, F. Tufail, M. W. Iqbal and S. K. Mukherjee, Investigated the Structural, Optoelectronic, Mechanical, and Thermoelectric Properties of Sr$_2$BTaO$_6$ (B = Sb, Bi) for Solar Cell Applications, *Int. J. Energy Res.*, 2022, **46**(15), 23698–23714, DOI: 10.1002/ er.8669.

78 A. Jabar, S. Idrissi and L. Bahmad, A DFT Study of the Structural, Electronic, Optical, Thermoelectric, and Thermodynamic Properties of the Halide Double Perovskite Cs$_2$CeCl$_6$, *J. Electroceram.*, 2025, **53**(2), 186–198, DOI: 10.1007/s10832-025-00382-4.

79 Q. Mahmood, U. Hani, T. I. Al-Muhimeed, A. A. AlObaid, B. Ul Haq, G. Murtaza, T. H. Flemban and H. Althib, Study of Optical and Thermoelectric Properties of ZYbI3 (Z = Rb, Cs) for Solar Cells and Renewable Energy; Modelling by Density Functional Theory, *J. Phys. Chem. Solids*, 2021, **155**, 110117, DOI: 10.1016/j.jpcs.2021.110117.

80 M. Tarekuzzaman, M. H. Ishraq, M. S. Parves, M. A. Rayhan, S. Ahmad, M. Rasheduzzaman, K. A. A. Mamun, M. M. Hossen and M. Z. Hasan, An In-Depth Investigation of Lead-Free KGeCl3 Perovskite Solar Cells Employing Optoelectronic, Thermomechanical, and Photovoltaic Properties: DFT and SCAPS-1D Frameworks, *Phys. Chem. Chem. Phys.*, 2024, **26**(43), 27704–27734, DOI: 10.1039/ D4CP02974G.

81 N. Singh, A. Agarwal and M. Agarwal, Numerical Simulation of Highly Efficient Lead-Free All-Perovskite Tandem Solar Cell, *Sol. Energy*, 2020, **208**, 399–410, DOI: 10.1016/ j.solener.2020.08.003.

82 H. B. Michaelson, The Work Function of the Elements and Its Periodicity, *J. Appl. Phys.*, 1977, **48**(11), 4729–4733, DOI: 10.1063/1.323539.

83 F. Behrouznejad, S. Shahbazi, N. Taghavinia, H.-P. Wu and E. W.-G. Diau, A Study on Utilizing Different Metals as the Back Contact of CH$_3$NH$_3$PbI$_3$ Perovskite Solar Cells, *J. Mater. Chem. A*, 2016, **4**(35), 13488–13498, DOI: 10.1039/ C6TA05938D.

84 K. Sekar, L. Marasamy, S. Mayarambakam, H. Hawashin, M. Nour and J. Bouclé, Lead-Free, Formamidinium Germanium-Antimony Halide (FA$_4$GeSbCl$_{12}$) Double Perovskite Solar Cells: The Effects of Band Offsets, *RSC Adv.*, 2023, **13**(36), 25483–25496, DOI: 10.1039/D3RA03102K.

85 C. Walkons, R. Murshed and S. Bansal, Numerical Analysis of Pb-Free Perovskite Absorber Materials: Prospects and Challenges, *Solar RRL*, 2020, **4**(10), 2000299, DOI: 10.1002/ solr.202000299.

86 T. Minemoto and M. Murata, Theoretical Analysis on Effect of Band Offsets in Perovskite Solar Cells, *Sol. Energy Mater. Sol. Cells*, 2015, **133**, 8–14, DOI: 10.1016/j.solmat.2014.10.036.

87 B. Qi and J. Wang, Fill Factor in Organic Solar Cells, *Phys. Chem. Chem. Phys.*, 2013, **15**(23), 8972–8982, DOI: 10.1039/ C3CP51383A.

88 M. Raihan Kabir, N. Shahadath, M. Tarekuzzaman, M. A. Bakkar Siddique, O. Alsalmi, M. Rasheduzzaman, M. Abdul Qader, M. Moazzam Hossen and M. Zahid Hasan, Computational Analysis of LiMgI3: A Promising Material for Solar Energy Conversion, *RSC Adv.*, 2025, **15**(23), 17906–17932, DOI: 10.1039/D5RA02550H.

89 M. S. Reza, A. Ghosh, Y. A. Kumar, M. A. Imran, K. Alam, M. M. Rahman, N. S. Awwad and H. A. Ibrahium, High-Efficiency and Eco-Friendly Cs$_2$SnBr$_6$-Based Perovskite Solar Cells: Optimized Device Architecture and Performance Analysis via SCAPS-1D

Simulation, *Opt. Express*, 2025, **33**(14), 30441–30462, DOI: 10.1364/OE.566116.

90 M. K. Hossain, A. A. Arnab, D. P. Samajdar, M. H. K. Rubel, M. M. Hossain, Md. R. Islam, R. C. Das, H. Bencherif, Md. F. Rahman, J. Madan, R. Pandey, S. Bhattarai, M. Amami and D. K. Dwivedi, Design Insights into La_2NiMnO_6-Based Perovskite Solar Cells Employing Different Charge Transport Layers: DFT and SCAPS-1D Frameworks, *Energy Fuels*, 2023, **37**(17), 13377–13396, DOI: 10.1021/acs.energyfuels. 3c02361.

91 L. Et-taya, T. Ouslimane and A. Benami, Numerical Analysis of Earth-Abundant $Cu_2ZnSn(S_xSe_{1-x})_4$ Solar Cells Based on Spectroscopic Ellipsometry Results by Using SCAPS-1D, *Sol. Energy*, 2020, **201**, 827–835, DOI: 10.1016/j.solener.2020. 03.070.

92 J. D. Servaites, S. Yeganeh, T. J. Marks and M. A. Ratner, Efficiency Enhancement in Organic Photovoltaic Cells: Consequences of Optimizing Series Resistance, *Adv. Funct. Mater.*, 2010, **20**(1), 97–104, DOI: 10.1002/adfm.200901107.

93 E. E. van Dyk and E. L. Meyer, Analysis of the Effect of Parasitic Resistances on the Performance of Photovoltaic Modules, *Renewable Energy*, 2004, **29**(3), 333–344, DOI: 10.1016/S0960-1481(03)00250-7.

94 O. K. Simya, A. Mahaboobbatcha and K. Balachander, A Comparative Study on the Performance of Kesterite Based Thin Film Solar Cells Using SCAPS Simulation Program, *Superlattices Microstruct.*, 2015, **82**, 248–261, DOI: 10.1016/j.spmi.2015.02.020.

95 Y. Li, B. Ding, Q.-Q. Chu, G.-J. Yang, M. Wang, C.-X. Li and C.-J. Li, Ultra-High Open-Circuit Voltage of Perovskite Solar Cells Induced by Nucleation Thermodynamics on Rough Substrates, *Sci. Rep.*, 2017, **7**(1), 46141, DOI: 10.1038/srep46141.

96 A. D. Dhass, E. Natarajan and L. Ponnusamy, Influence of Shunt Resistance on the Performance of Solar Photovoltaic Cell, *2012 International Conference on Emerging Trends in Electrical Engineering and Energy Management (ICETEEEM)*, 2012, pp. 382–386, DOI: 10.1109/ICETEEEM.2012.6494522.

97 A. Sunny, S. Rahman, M. M. Khatun and S. R. A. Ahmed, Numerical Study of High Performance HTL-Free $CH_3NH_3SnI_3$-Based Perovskite Solar Cell by SCAPS-1D, *AIP Adv.*, 2021, **11**(6), 065102, DOI: 10.1063/5.0049646.

98 Md. F. Hossain, A. Ghosh, M. A. Al Mamun, A. A. Miazee, H. Al-lohedan, R. J. Ramalingam, M. F. I. Buian, S. R. I. Karim, Md. Y. Ali and M. Sundararajan, Design and Simulation Numerically with Performance Enhancement of Extremely Efficient Sb_2Se_3-Based Solar Cell with V_2O_5 as the Hole Transport Layer, Using SCAPS-1D Simulation Program, *Opt. Commun.*, 2024, **559**, 130410, DOI: 10.1016/j.optcom.2024.130410.

99 S. R. Raga, E. M. Barea and F. Fabregat-Santiago, Analysis of the Origin of Open Circuit Voltage in Dye Solar Cells, *J. Phys. Chem. Lett.*, 2012, **3**(12), 1629–1634, DOI: 10.1021/jz3005464.

100 A. Ghosh, A. S. Zishan, M. Moumita, Y. A. Kumar, A. K. Roy, S. Islam, S. Ahmed, H. Z. Anonto, A. T. Happy,

M. Shameem Ahsan, H. A. Alrafai and A. A. Hassan, Improving the Performance of AgCdF3-Based Perovskite Solar Cells Using Machine Learning-Driven Adjustment of Active Layer and Charge Transport Materials with SCAPS-1D, *Inorg. Chem. Commun.*, 2025, **179**, 114829, DOI: 10.1016/j.inoche.2025.114829.

101 S. Lin, Computer Solutions of the Traveling Salesman Problem, *Bell Syst. Tech. J.*, 1965, **44**(10), 2245–2269, DOI: 10.1002/j.1538-7305.1965.tb04146.x.

102 X. Zhang, X. Chen, Y. Chen, N. A. N. Ouedraogo, J. Li, X. Bao, C. Bao Han, Y. Shirai, Y. Zhang and H. Yan, Rapid degradation behavior of encapsulated perovskite solar cells under light, bias voltage or heat fields, *Nanoscale Adv.*, 2021, **3**(21), 6128–6137, DOI: 10.1039/D1NA00495F.

103 E. H. Jung, N. J. Jeon, E. Y. Park, C. S. Moon, T. J. Shin, T.-Y. Yang, J. H. Noh and J. Seo, Efficient, Stable and Scalable Perovskite Solar Cells Using Poly(3-Hexylthiophene), *Nature*, 2019, **567**(7749), 511–515, DOI: 10.1038/s41586-019-1036-3.

104 M. K. Hossain, D. P. Samajdar, R. C. Das, A. A. Arnab, Md. F. Rahman, M. H. K. Rubel, Md. R. Islam, H. Bencherif, R. Pandey, J. Madan and M. K. A. Mohammed, Design and Simulation of Cs_2BiAgI_6 Double Perovskite Solar Cells with Different Electron Transport Layers for Efficiency Enhancement, *Energy Fuels*, 2023, **37**(5), 3957–3979, DOI: 10.1021/acs.energyfuels.3c00181.

105 Mamta, K. K. Maurya and V. N. Singh, Sb_2Se_3/CZTS Dual Absorber Layer Based Solar Cell with 36.32% Efficiency: A Numerical Simulation, *J. Sci.: Adv. Mater. Devices*, 2022, **7**(2), 100445, DOI: 10.1016/j.jsamd.2022.100445.

106 J. R. Macdonald, W. B. Johnson, I. D. Raistrick, D. R. Franceschetti, N. Wagner, M. C. H. McKubre, D. D. Macdonald, B. Sayers, N. Bonanos, B. C. H. Steele, E. P. Butler, W. L. Worell, G. A. Niklasson, S. Malmgren, M. Stromme, S. K. Sundaram, G. R. Engelhardt, E. Barsoukov, B. E. Conway, W. G. Pell, C. M. Roland and R. S. Eisenberg, in *Impedance Spectroscopy: Theory, Experiment, and Applications*, ed. E. Barsoukov and J. R. Macdonald, John Wiley & Sons, 3rd edn, 2018, pp. 424–458.

107 S. Bhattarai, R. Pandey, J. Madan, S. Tayeng, P. K. Kalita, M. Zahid Ansari, L. B. Farhat, M. Amami and M. Khalid Hossain, Comparative Study of Distinct Halide Composites for Highly Efficient Perovskite Solar Cells Using a SCAPS-1D Simulator, *RSC Adv.*, 2023, **13**(38), 26851–26860, DOI: 10.1039/D3RA04134D.

108 E. von Hauff and D. Klotz, Impedance Spectroscopy for Perovskite Solar Cells: Characterisation, Analysis, and Diagnosis, *J. Mater. Chem. C*, 2022, **10**(2), 742–761, DOI: 10.1039/D1TC04727B.

109 N. Neelu, N. Pandey and S. Chakrabarti, Synthesis, Structural and Optical Properties of Lead Free $Cs_2CuBiCl_6$: A Potential & Promising Eco-Friendly Double Perovskite for Solar Cell Applications, *Opt. Mater.*, 2023, **143**, 114250, DOI: 10.1016/j.optmat.2023.114250.

110 E. Greul, M. L. Petrus, A. Binek, P. Docampo and T. Bein, Highly Stable, Phase Pure $Cs_2AgBiBr_6$ Double Perovskite

Thin Films for Optoelectronic Applications, *J. Mater. Chem. A*, 2017, **5**(37), 19972–19981, DOI: 10.1039/C7TA06816F.

111 M. T. Islam, M. R. Jani, S. M. Al Amin, M. S. U. Sami, K. M. Shorowordi, M. I. Hossain, M. Devgun, S. Chowdhury, S. Banerje and S. Ahmed, Numerical Simulation Studies of a Fully Inorganic $Cs_2AgBiBr_6$ Perovskite Solar Device, *Opt. Mater.*, 2020, **105**, 109957, DOI: 10.1016/j.optmat.2020.109957.

112 R. Yao, S. Ji, T. Zhou, C. Quan, W. Liu and X. Li, Self-energy correction and numerical simulation for efficient lead-free double perovskite solar cells, *Phys. Chem. Chem. Phys.*, 2024, **26**(6), 5253–5261, DOI: 10.1039/D3CP03639A.

113 F. Igbari, R. Wang, Z.-K. Wang, X.-J. Ma, Q. Wang, K.-L. Wang, Y. Zhang, L.-S. Liao and Y. Yang, Composition Stoichiometry of $Cs_2AgBiBr_6$ Films for Highly Efficient Lead-Free Perovskite Solar Cells, *Nano Lett.*, 2019, **19**(3), 2066–2073, DOI: 10.1021/acs.nanolett.9b00238.

114 M. S. Shadabroo, H. Abdizadeh and M. R. Golobostanfard, Dimethyl Sulfoxide Vapor-Assisted $Cs_2AgBiBr_6$ Homogenous Film Deposition for Solar Cell Application, *ACS Appl. Energy Mater.*, 2021, **4**(7), 6797–6805, DOI: 10.1021/acsaem.1c00894.

115 M. Shirazi, Optimizing Key Parameters to Enhance the Performance of Lead-Free Perovskite Solar Cells with a $Cs_2AgBiCl_6$ Absorber Layer Using SCAPS-1D Simulation, *J. Opt.*, 2025, 1–18, DOI: 10.1007/s12596-025-02557-2.

116 Jyoti and D. Muchahary, Numerical Analysis of $K_2CuBiBr_6$ for Enhanced Solar Cell Performance Potential, *Modell. Simul. Mater. Sci. Eng.*, 2025, **33**(4), 045018, DOI: 10.1088/1361-651X/add94f.

117 S. Srivastava, A. K. Singh, P. Kumar and B. Pradhan, Comparative Performance Analysis of Lead-Free Perovskites Solar Cells by Numerical Simulation, *J. Appl. Phys.*, 2022, **131**(17), 175001, DOI: 10.1063/5.0088099.

© 2026 The Author(s). Published by the Royal Society of Chemistry